# Background–source separation in astronomical images with Bayesian probability theory – I. The method

F. Guglielmetti,[*] R. Fischer and V. Dose

*Max-Planck-Institut für Plasmaphysik, Boltzmannstrasse 2, 85748 Garching, Germany*

**ABSTRACT**

A probabilistic technique for the joint estimation of background and sources with the aim of detecting faint and extended celestial objects is described. Bayesian probability theory is applied to gain insight into the co-existence of background and sources through a probabilistic two-component mixture model, which provides consistent uncertainties of background and sources. A multiresolution analysis is used for revealing faint and extended objects in the frame of the Bayesian mixture model. All the revealed sources are parametrized automatically providing source position, net counts, morphological parameters and their errors.

We demonstrate the capability of our method by applying it to three simulated data sets characterized by different background and source intensities. The results of employing two different prior knowledge on the source signal distribution are shown. The probabilistic method allows for the detection of bright and faint sources independently of their morphology and the kind of background. The results from our analysis of the three simulated data sets are compared with other source detection methods. Additionally, the technique is applied to *ROSAT* All-Sky Survey data.

**Key words:** methods: data analysis – methods: statistical – techniques: image processing.

## 1 INTRODUCTION

Background estimation is an omnipresent problem for source detection methods in astrophysics, especially when the source signal is weak and difficult to discriminate against the background. An inaccurate estimation of the background may produce large errors in object photometry and the loss of faint and/or extended objects.

Deep observations are commonly obtained by combining several individual exposures to generate a final astronomical image. Often large exposure variations characterize these data and the background may vary significantly within the field. Hence, the background modelling has to incorporate the knowledge provided by the observatory's exposure time without compromising the statistical properties. In addition, instrumental structures, such as detector ribs or CCD gaps, produce lack of data. The missing data must be handled consistently in the background estimation to prevent undesired artificial effects.

Celestial objects exhibit a large variety of morphologies and apparent sizes. Thus, the search for sources should not be driven by any predefined morphology, allowing proper estimate of their structural parameters. The instrumental point spread function (PSF) is often not known exactly for the whole field of view. So a source detection algorithm should be able to operate effectively without the knowledge of the instrument characteristics.[1]

Conventional source detection methods employed in deep imaging surveys are SEXTRACTOR (Bertin & Arnouts 1996), sliding window technique (Harnden et al. 1984; Gioia et al. 1990) and maximum likelihood PSF fitting (Hasinger, Johnston & Verbunt 1994; Boese & Doebereiner 2001), wavelet transformation (e.g. Slezak, Bijaoui & Mars 1990; Rosati et al. 1995; Damiani et al. 1997; Starck & Pierre 1998; Freeman et al. 2002). A review of these techniques can be found in Valtchanov, Pierre & Gastaud (2001) and Becker et al. (2007).

SEXTRACTOR is one of the most widely used source detection procedure in astronomy. It has a simple interface and very fast execution. It produces reliable aperture photometry catalogues (Becker et al. 2007). It is applied in *X*-ray regime on filtered images (Valtchanov et al. 2001).

The sliding window technique is a fast and robust source detection method. This technique may fail while detecting extended sources, sources near the detection limit and nearby sources (Valtchanov et al. 2001). This source detection method has been refined with more elaborated techniques, such as matched filters (e.g. Vikhlinin

---

[1] If the instrumental PSF is known precisely, then that information can be taken into account in a further step of source characterization within the properties of a specific observational set-up.

[*]E-mail: Fabrizia.Guglielmetti@ipp.mpg.de

et al. 1995; Stewart 2006) and recently the Cash method (Stewart 2009). The Cash method is a maximum likelihood technique. For source detection, the method employs a Cash likelihood-ratio statistic, that is an extended $\chi^2$ statistic for Poisson data (Cash 1979). Both the matched filters and Cash methods are at least by a factor of 1.2 more sensitive than the sliding window technique (Stewart 2009). Though, both methods are designed for the detection of point sources. The candidate sources are characterized in a further step using maximum likelihood PSF fitting. The maximum likelihood PSF fitting procedure performs better than other conventional techniques for flux measurements of point-like sources although accurate photometry is achieved when the PSF model used is close to the image PSF (Valtchanov et al. 2001). In Pierre et al. (2004), the maximum likelihood profile fit on photon images is extended taking into account a spherically symmetric $\beta$-model (King profile; see King 1962; Cavaliere & Fusco-Femiano 1978) convolved with the instrumental PSF for improving the photometry of extended objects.

Wavelet transform (WT) techniques improve the detection of faint and extended sources with respect to other conventional methods (see Starck & Pierre 1998 for more details). In fact, WT techniques are able to discriminate structures as a function of scale. Within larger scales, faint and extended sources are revealed. WTs are therefore valuable tools for the detection of both point-like and extended sources (Valtchanov et al. 2001). None the less, these techniques favour the detection of circularly symmetric sources (Valtchanov et al. 2001). In addition, artefacts may appear around the detected structures in the reconstructed image, and the flux is not preserved (Starck & Pierre 1998). In order to overcome these problems, some refinements have been applied to the WT techniques. Starck & Pierre (1998), for instance, employ a multiresolution support filtering to preserve the flux and the adjoint WT operator to suppress artefacts which may appear around the objects. An advance on this method is presented in Starck et al. (2000). A space-variant PSF is incorporated in their WT technique. Object by object reconstruction is performed. For point sources the flux measurements are close to that obtained by PSF fitting.

The detection of faint extended and point-like sources is a nontrivial task for source detection methods. This task becomes more complicated when the detection rate and photometric reconstruction for the sources are taken into account (Valtchanov et al. 2001).

A self-consistent statistical approach for background estimation and source detection is given by Bayesian probability theory (BPT), which provides a general and consistent frame for logical inference. The achievement of Bayesian techniques on signal detections in astrophysics has already been shown, for example in the works of Gregory & Loredo (1992), Loredo & Wasserman (1995) and Scargle (1998). In modern observational astrophysics, BPT techniques for image analysis have been extensively applied e.g. Hobson & McLachlan (2003), Strong (2003), Savage & Oliver (2007) and Carvalho, Rocha & Hobson (2009). For the detection of discrete objects embedded in Gaussian noise (microwave regime), Hobson & McLachlan (2003) utilizes a model-fitting methodology, where a parametrized form for the objects of interest is assumed. Markov-chain Monte Carlo (MCMC) techniques are used to explore the parameter space. An advance on this work is provided by Carvalho et al. (2009). For speeding up the method of Hobson & McLachlan (2003), Carvalho et al. (2009) proposes to use Gaussian approximation to the posterior probability density function (pdf) peak when performing a Bayesian model selection for source detection. The work of Savage & Oliver (2007) is developed within Gaussian statistics (infrared data). At each pixel position in an image, their method

estimates the probability of the data being described by point source or empty sky under the assumptions that the background is uniform and the sources have circular shapes. The Bayesian information criterion is used for the selection of the two models. Source parameters are estimated in a second step employing Bayesian model selection. Strong (2003) developed a technique for image analysis within Poisson statistics. The technique is instrument specific and is applied to $\gamma$-ray data. The first objective of this technique is to reconstruct the intensity in each image pixel given a set of data. The maximum entropy method is used for selecting from the data an image between all the available ones from a multidimensional space. The dimension of the space is proportional to the number of image pixels.

We propose a new source detection method based on BPT combined with the mixture-model technique. The algorithm allows one to estimate the background and its uncertainties and to detect celestial sources jointly. The new approach deals directly with the statistical nature of the data. Each pixel in an astronomical image is probabilistically assessed to contain background only or with additional source signal. The results are given by probability distributions quantifying our state of knowledge. The developed background–source separation (BSS) method encounters background estimation, source detection and characterization.

The background estimation incorporates the knowledge of the exposure time map. The estimation of the background and its uncertainties is performed on the full astronomical image employing a two-dimensional spline. The spline models the background rate. The spline amplitudes and the position of the spline supporting points provide flexibility in the background model. This procedure can describe both smoothly and highly varying backgrounds. Hence, no cut out of regions or employment of meshes are needed for the background estimation. The BSS technique does not need a threshold level for separating the sources from the background as conventional methods do. The threshold level is replaced by a measure of probability. In conventional methods, the threshold level is described in terms of the noise standard deviation, then translated into a probability. The classification assigned to each pixel of an astronomical image with the BSS method allows one to detect sources without employing any predefined morphologies. Only, for parametric characterization of the sources predefined source shapes are applied. The estimation of source parameters and their uncertainties includes the estimated background into a forward model. Only the statistics of the original data are taken into account. The BSS method provides simultaneously the advantages of a multiresolution analysis and a multicolour detection. Objects in astronomical images are organized in hierarchical structures (Starck & Murtagh 2006). In order to quantify the multiscale structure in the data, a multiresolution analysis is required (see Kolaczyk & Dixon 2000; Starck et al. 2000). In the BSS approach the multiresolution analysis is incorporated in combination with the source detection and background estimation technique with the aim to analyse statistically source structures at multiple scales. When multiband images are available, the information contained in each image can be statistically combined in order to extend the detection limit of the data (see Szalay, Connolly & Szokoly 1999; Murtagh, Raftery & Starck 2005).

The capabilities of this method are best shown with the detections of faint sources independently of their shape and with the detections of sources embedded in a highly varying background. The technique for the joint estimation of background and sources in digital images is applicable to digital images collected by a wide variety of sensors at any wavelength. The X-ray environment is

particularly suitable to our Bayesian approach for different reasons. First, X-ray astronomy is characterized by low photon counts even for relatively large exposures and the observational data are unique, i.e. the experiment is rarely reproduced. Second, the X-ray astronomical images provided by new generation instruments are usually a combination of several individual CCD imaging pointings. Last, there are few source detection algorithms developed so far for an automated search of faint and extended sources.

In this paper, our aim is to describe the developed BSS technique. The outline of this paper is as follows. In Section 2, we briefly review the basic aspects of BPT. In Section 3, we introduce the background estimation and source detection technique. In Section 4, the BSS algorithm is extended in order to obtain an automated algorithm for source characterization. In Section 5, the issue of false positives in source detection is addressed. In Section 6, the BSS method is applied to simulated data. We show results for two different choices of prior pdf for the source signal. In Section 7, our results on the three simulated data sets are compared with the outcome from WAVDETECT algorithm (Freeman et al. 2002). In Section 8, we test the BSS method on astronomical images coming from *ROSAT* All-Sky Survey (RASS) data. Our conclusions on the BSS technique are provided in Section 9. In Section 10, a list of acronyms used throughout the paper is reported.

The flexibility of our Bayesian technique allows the investigation of data coming from past and modern instruments without changes in our algorithm. An extensive application of the BSS technique to real data is addressed in a forthcoming paper (Guglielmetti et al., in preparation). In the latter, the BSS algorithm is used for the analysis of a specific scientific problem, i.e. the search of galaxy clusters in the CDF-S data.

## 2 BAYESIAN PROBABILITY THEORY

In order to analyse the heterogeneous data present in astronomical images, we employ BPT (see Jeffreys 1961; Bernardo & Smith 1994; Gelman et al. 1995; Sivia 1996; Dose 2003; Jaynes 2003; O'Hagan & Forster 2004; Gregory 2005). BPT gives a calculus how to resolve an inference problem based on uncertain information. The outcome of the BPT analysis is the pdf of the quantity of interest, which encodes the knowledge to be drawn from the information available (a posteriori). The posterior pdf comprises the complete information which can be inferred from the data and the statistical model, and supplementary information such as first-principle physics knowledge.

This statistical approach is based on comparisons among alternative hypotheses (or models) using the single observed data set. Each information entering the models that describe the data set is combined systematically. The combination includes all data sets coming from different diagnostics, physical model parameters and measurement nuisance parameters. Each data set and parameters entering the models are subject to uncertainties which have to be estimated and encoded in probability distributions. Within BPT the so-called statistical and systematic uncertainties are not distinguished. Both kinds of uncertainties are treated as a lack of knowledge.

Bayes' theorem states

$$P(H_i|D, \sigma, I) = \frac{P(D|H_i, \sigma, I)P(H_i|I)}{P(D|I)}, \qquad (1)$$

where the number of alternative hypotheses to be compared is larger than or equal to 2. Bayes' theorem is a consequence of the sum and product rules of probability theory. The vertical bars in (1) denote conditionality property, based on either empirical or theoretical in-

formation. Equation (1) relates the *posterior* pdf $P(H_i|D, \sigma, I)$ to known quantities, namely, the *likelihood* pdf $P(D|H_i, \sigma, I)$ and the *prior* pdf $P(H_i|I)$. $P(D|I)$ is the *evidence* of the data which constitutes the normalization and will not affect the conclusions within the context of a given model. The posterior pdf is the quantity to be inferred. It depends on the full data set $D$, on the errors $\sigma$ entering the experiment and on all relevant information concerning the nature of the physical situation and knowledge of the experiment ($I$). The likelihood pdf represents the probability of finding the data $D$ for given quantities of interest, uncertainties $\sigma$ and additional information $I$. It reveals the error statistics of the experiment. The prior pdf is independent from the experimental errors. It represents physical constraints or additional information from other diagnostics. The terms 'posterior' and 'prior' have a logical rather than temporal meaning. The posterior and prior pdfs can be regarded as the knowledge 'with' and 'without' the new data taken into account, respectively.

In order to arrive at the pdf of any quantity $x$ in the model, marginalization of the multidimensional pdf can be regarded as a projection of the complete pdf on to that quantity. Marginalization is performed by integration over the quantity $y$ one wants to get rid of

$$P(x) = \int P(x, y)\, dy = \int P(x|y)P(y)\, dy. \qquad (2)$$

Marginalization of a quantity $y$ thus takes into account the uncertainty of $y$ which is quantified by the pdf $P(y)$. The uncertainty of $y$ propagates into the pdf $P(x)$. Marginalization provides a way to eliminate variables which are necessary to formulate the likelihood but otherwise uninteresting.

Another important property of BPT is the capability of modelling the data by mixture distributions in the parameter space (Everitt & Hand 1981; Neal 1992). Mixture distributions are an appropriate tool for modelling processes whose output is thought to be generated by several different underlying mechanisms, or to come from several different populations. Our aim is to identify and characterize these underlying 'latent classes'. Therefore, we follow the standard Bayesian approach to this problem, which is to define a prior distribution over the parameter space of the mixture model and combine this with the observed data to give a posterior distribution over the parameter space. Essential for model comparison or object classification is the marginal likelihood (*evidence*, *prior predicted value*). Marginalization (integration) of the likelihood over parameter space provides a measure for the credibility of a model for given data. Ratios of marginal likelihoods (*Bayes factors*) are frequently used for comparing two models (Kass & Raftery 1995). Details of mixture modelling in the framework of BPT can be found in von der Linden, Dose & Fischer (1997), von der Linden et al. (1999), Fischer et al. (2000, 2001) and Fischer & Dose (2002). In particular, Fischer & Dose (2002) have demonstrated the capability of the Bayesian mixture model technique even with an unknown number of components for background separation from a measured spectrum. The present approach follows these previous works.

## 3 THE JOINT ESTIMATION OF BACKGROUND AND SOURCES WITH BPT

The aim of the BSS method is the joint estimation of background and sources in two-dimensional image data. We can identify two basic steps of our algorithm: (A) background estimation and source detection, (B) calculation of source probability maps in a multiresolution analysis.

The input information of the developed algorithm is the experimental data, i.e. the detected photon counts, and the observatory's exposure time.

The background rate is assumed to be smooth, e.g. spatially slowly varying compared to source dimensions. To allow for smoothness the background rate is modelled with a two-dimensional thin-plate spline (TPS) (Section 3.2). The number and the positions of the pivots, i.e. the spline's supporting points, decide what data structures are assigned to be background. All structures which cannot be described by the background model will be assigned to be sources. The number of pivots required to model the background depends on the characteristics of the background itself. Though the minimum number of pivots is four (since the minimum expansion of the selected spline has four terms), their number increases with increasing background variation.

The co-existence of background and sources is described with a probabilistic two-component mixture model (Section 3.1) where one component describes background contribution only and the other component describes background plus source contributions. Each pixel is characterized by the probability of belonging to one of the two mixture components. For the background estimation the photons contained in all pixels are considered including those containing additional source contributions. No data censoring by cutting out source areas are employed.

For background estimation the source intensity is considered to be a nuisance parameter. According to the rules of BPT, the source signal distribution is described probabilistically in terms of a prior pdf. The prior pdf of the source signal is an approximation to the true distribution of the source signal on the field. We studied two prior pdfs of the source signal: the exponential and the inverse-Gamma function.

The background and its uncertainties (Section 3.3) are estimated from its posterior pdf. Therefore, for each pixel of an astronomical image an estimate of its background and its uncertainties is provided.

Moreover, the Bayesian approach introduces hyperparameters, that are fundamental for the estimation of the posterior pdfs for the background and source intensities. Specifically, in Section 3.4 we show that the hyperparameters are estimated exclusively from the data.

The source probability is evaluated with the mixture model technique for pixels and pixel cells[2] in order to enhance the detection of faint and extended sources in a multiresolution analysis. Pixels and pixel cells are treated identically within the Bayesian formalism. For the correlation of neighbouring pixels, the following methods have been investigated: box filter with a square, box filter with a circle, Gaussian weighting filter (see Section 3.1 for more details).

The BSS technique is morphology free, i.e. there are no restrictions on the object size and shape for being detected. An analysed digital astronomical image is converted into the following:

(I) the background rate image, or *'TPS map'*, is an array specifying the estimated background rate at each image pixel for a given observation. The effects of exposure variations are consistently included in the spline model;

(II) the background image, or *'background map'*, is an array specifying the estimated background amplitude at each image pixel

for a given observation. It is provided by the TPS map multiplied with the telescope's exposure;

(III) the source probability images, or *'source probability maps'* (SPMs), display the probability that source counts are present in pixels and pixel cells for a given observation in a multiresolution analysis.

Movies are produced with the SPMs obtained at different resolutions. The moving images allow one to discern interactively the presence of faint extended sources in digital astronomical images. The size of faint extended sources is correlated with the scale of the resolution, used for their detection. SPMs coming from other energy bands can be combined statistically to produce conclusive SPMs at different resolutions with the advantage to provide likelihoods for the detected sources from the combined energy bands (Section 3.5.1).

### 3.1 Two-component mixture model

The general idea of the described Bayesian model is that a digital astronomical image consists of a smooth background with additive source signal, which can be characterized by any shape, size and brightness. The background signal is the diffuse cosmic emission added to the instrumental noise. The source signal is the response of the imaging system to a celestial object. A surface $b(\boldsymbol{x})$ describes the background under the source signal, where $\boldsymbol{x} = (x, y)$ corresponds to the position on the grid in the image.

Therefore, given the observed data set $D = \{d_{ij}\} \in \mathbf{N}_0$, where $d_{ij}$ is photon counts in pixel (or pixel cell) $\{i j\}$, two complementary hypotheses arise:

$$\begin{cases} B_{ij} : & d_{ij} = b_{ij} + \epsilon_{ij}, \\ \overline{B}_{ij} : & d_{ij} = b_{ij} + s_{ij} + \epsilon_{ij}. \end{cases}$$

Hypothesis $B_{ij}$ specifies that the data $d_{ij}$ consists only of background counts $b_{ij}$ spoiled with noise $\epsilon_{ij}$, i.e. the (statistical) uncertainty associated with the measurement process. Hypothesis $\overline{B}_{ij}$ specifies the case where additional source intensity $s_{ij}$ contributes to the background. Additional assumptions are that no negative values for source and background amplitudes are allowed and that the background is smoother than the source signal.

The smoothness of the background is achieved by modelling the background count rate with a bivariate TPS where the supporting points are chosen sparsely to ensure that sources cannot be fitted. The spline fits the background component whereas count enhancements classify pixels and pixel cells with source contributions.

In the following, pixel cells are subsumed by pixels. Pixel cells are collections of pixels where $d_{ij}$ is the total photon count in the cell $\{i j\}$. The photon counts of neighbouring pixels are added up and the formed pixel cell is treated as a pixel. In principle, any cell shape can be chosen. In practice, two methods have been developed when pixels have weight of one within the cell (box filtering with cell shape of a square or of a circle) and one method when pixels have different weights within the cell (Gaussian weighting). The box filter with cells of squared shape consists of taking information of neighbouring pixels within a box. The cell size is the box size. The box filter with cells of circular shape considers pixels with a weight of one if inside the cell size, otherwise zero. Pixels have a weight of one when the cell size touches them at least at the centre. This method allows the pixel cells to have varying shapes. The Gaussian weighting method provides Gaussian weights around a centre: weights are given at decreasing values according to the distance from the centre.

---

[2] We define pixels as the image finest resolution limited by instrumental design, while we define pixel cells as a group of correlated neighbouring pixels.

As expressed in (1), we are interested in estimating the probabilities of the hypotheses: $B_{ij}$ and $\overline{B}_{ij}$.

In this paper we address the problem when the photon counts are small and Poisson statistics have to be used. The likelihood probabilities for the two hypotheses within Poisson statistics are

$$p(d_{ij} \mid B_{ij}, b_{ij}) = \frac{b_{ij}^{d_{ij}}}{d_{ij}!} \, e^{-b_{ij}}, \qquad (3)$$

$$p(d_{ij} \mid \overline{B}_{ij}, b_{ij}, s_{ij}) = \frac{(b_{ij} + s_{ij})^{d_{ij}}}{d_{ij}!} \, e^{-(b_{ij}+s_{ij})}. \qquad (4)$$

This technique is easily adaptable to other likelihoods, for instance employing Gaussian statistics as given in Fischer et al. (2001).

The prior pdfs for the two complementary hypotheses are chosen to be $p(B_{ij}) = \beta$ and $p(\overline{B}_{ij}) = 1 - \beta$, independent of i and j. Specifically, the parameter $\beta$ is the prior probability that a pixel contains only background.

Since it is not known if a certain pixel (or pixel cell) contains purely background or additional source signal, the likelihood for the mixture model is employed. The likelihood for the mixture model effectively combines the probability distributions for the two hypotheses, $B_{ij}$ and $\overline{B}_{ij}$:

$$p(D|\boldsymbol{b}, \boldsymbol{s})$$
$$= \prod_{ij} \left\{ \beta \frac{b_{ij}^{d_{ij}}}{d_{ij}!} \, e^{-b_{ij}} + (1 - \beta) \frac{(b_{ij} + s_{ij})^{d_{ij}}}{d_{ij}!} \, e^{-(b_{ij}+s_{ij})} \right\}, \qquad (5)$$

where $\boldsymbol{b} = \{b_{ij}\}$, $\boldsymbol{s} = \{s_{ij}\}$ and $\{i\,j\}$ corresponds to the pixels of the complete field.

The probability of having source contribution in pixels and pixel cells is according to Bayes' theorem (see Fischer et al. 2001):

$$p(\overline{B}_{ij} \mid d_{ij}, b_{ij}, s_{ij})$$
$$= \frac{(1 - \beta)\, p(d_{ij} \mid \overline{B}_{ij}, b_{ij}, s_{ij})}{\beta\, p(d_{ij} \mid B_{ij}, b_{ij}) + (1 - \beta)\, p(d_{ij} \mid \overline{B}_{ij}, b_{ij}, s_{ij})}. \qquad (6)$$

This equation enables the data contained in an astronomical image to be classified in two groups: with and without source signal contribution.

Equation (6) is also used in the multiresolution analysis. The SPM with the largest resolution is characterized by the probability of uncorrelated pixels. At decreasing resolutions a correlation length is defined. Starting from a value of 0.5, the correlation length increases in steps of 0.5 pixel for decreasing resolution. The SPMs at decreasing resolutions are, therefore, characterized by the information provided by background and photon counts in pixel cells. Specifically, photon counts and background counts are given by a weighted integration over pixel cells. The integrated photon and background counts enter the likelihood for the mixture model. Then, the source probability is estimated for each image pixel in the multiresolution analysis. The multiresolution algorithm preserves Poisson statistics.

### 3.1.1 Source signal as a nuisance parameter

Following Fischer et al. (2000, 2001), the source signal in (4) is a nuisance parameter, which is removed by integrating it out (marginalization rule, equation 2):

$$p(d_{ij}|\overline{B}_{ij}, b_{ij}) = \int_0^\infty p(d_{ij}|\overline{B}_{ij}, b_{ij}, s_{ij})\, p(s_{ij}|\overline{B}_{ij}, b_{ij})\, ds_{ij}.$$

A nuisance parameter is a parameter which is important for the model (describing the data), but it is not of interest at the moment.
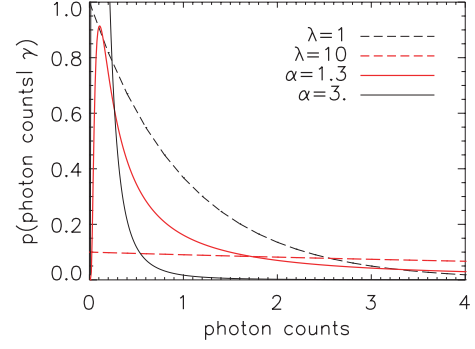


**Figure 1.** Representation of selected prior pdfs of the source signal versus the photon counts. The *exponential prior* pdf is drawn at two $\lambda$ values (dashed lines). The *inverse-Gamma function prior* pdf is plotted at two $\alpha$ values (continuous lines). On the ordinate, $\gamma$ indicates $\lambda$ or $\alpha$.

Following BPT, a prior pdf of the source signal has to be chosen. The final result depends crucially on the prior pdf set on the source signal. In fact, in addition to the choice of the TPS pivots, the prior pdf of the source signal provides a description of what is source. All that is not described as a source is identified as background and vice versa. Two approaches are presented: the first method accounts for the knowledge of the mean value of the source intensity over the complete field (*exponential prior*), the second approach interprets the source signal distribution according to a power law (*inverse-Gamma function prior*).

3.1.1.1 *Exponential prior* Following the works of Fischer et al. (2000, 2001) and Fischer & Dose (2002), we choose a prior pdf of the source signal that is as weakly informative as possible. The idea follows a practical argument on the difficulty of providing sensible information. We describe the prior pdf on the source intensity by an exponential distribution,

$$p(s_{ij} \mid \lambda) = \frac{e^{-(s_{ij}/\lambda)}}{\lambda}. \qquad (7)$$

This is the most uninformative maximum entropy distribution for known mean value of the source intensity $\lambda$ over the complete field.

In Fig. 1, equation (7) is drawn for two values of the mean source intensity: $\lambda = 1$ and 10 counts. No bright sources are expected to appear in fields with $\lambda \sim 1$. In the case of values of $\lambda \gg 1$, bright and faint sources are present in these fields.

The *marginal Poisson likelihood* for the hypothesis $\overline{B}_{ij}$ has the form

$$p(d_{ij}|\overline{B}_{ij}, b_{ij}, \lambda)$$
$$= \frac{e^{\frac{b_{ij}}{\lambda}}}{\lambda \left(1 + \frac{1}{\lambda}\right)^{(d_{ij}+1)}} \cdot \frac{\Gamma\left[(d_{ij}+1), b_{ij}\left(1 + \frac{1}{\lambda}\right)\right]}{\Gamma(d_{ij}+1)} \qquad (8)$$

where $\Gamma[a, x] = \int_x^\infty e^{-t} t^{a-1}\, dt\, (a > 0)$ is the incomplete-Gamma function and $\Gamma[a] = \Gamma[a, 0]$ is the Gamma function (see Fischer et al. 2000, 2001).

The behaviour of the Poisson and the marginal Poisson distributions is depicted with a parameter study. For the parameter study three background amplitudes $b$ are chosen: 0.1, 1 and 10 counts. In Fig. 2 the Poisson distribution (3) and the marginal Poisson distribution (8) are drawn on a logarithmic scale. These plots are indicated with (a), (b) and (c), respectively. The parameter $\lambda$, which describes
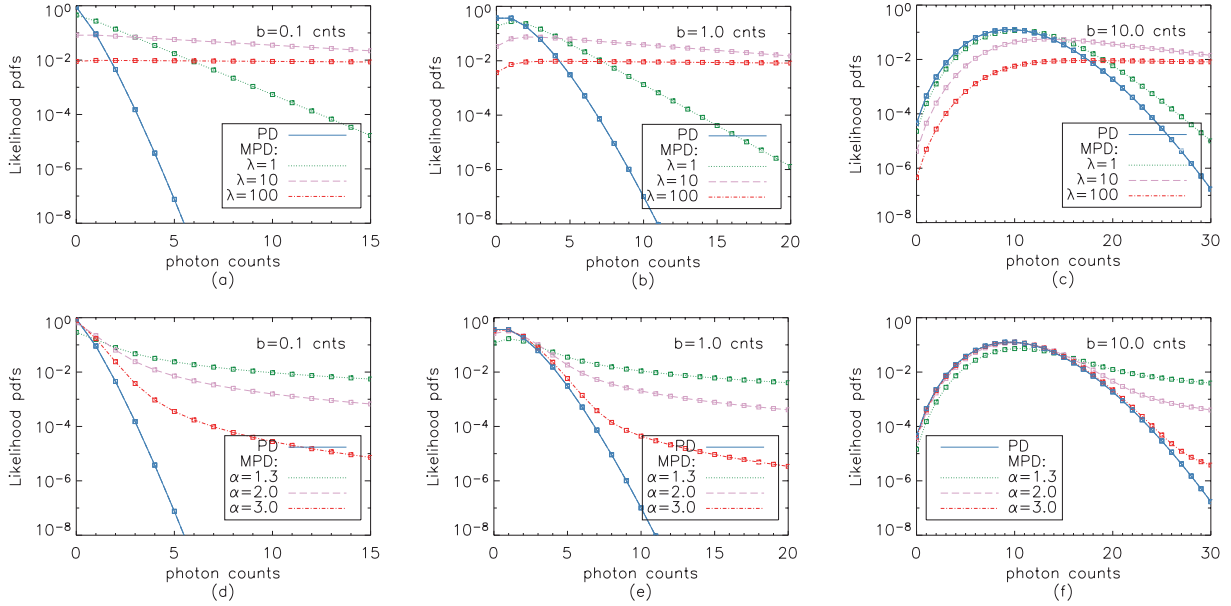
**Figure 2.** Likelihood pdfs versus photon counts. The Poisson distribution is indicated with PD. The marginal Poisson distribution is indicated with MPD. Panels (a)–(c) are obtained using the *exponential prior* pdf. Panels (d)–(f) are created using the *inverse-Gamma function prior* pdf.

the mean intensity in a field, has values of 1, 10 and 100 counts. The selected values for the background and for the parameter $\lambda$ are chosen such that the large variety of cases one encounters analysing digital astronomical images are covered. For instance, $b = 10$ counts and $\lambda = 1$ count (plot c) corresponds to a field when the source signal is much smaller than the background signal. On the other side, $b = 0.1$ counts and $\lambda = 100$ counts (plot a) corresponds to a field characterized by bright sources and small background amplitude.

The Poisson distribution is larger than the marginal Poisson distribution for photon counts lower than or equal to the background intensity. Hence, hypothesis $B_{ij}$ is more likely than the complementary hypothesis $\overline{B}_{ij}$. This situation changes when the photon counts are larger than the background amplitude.

The decay length of the marginal Poisson distribution is determined by the expected source intensity $\lambda$. The probability to detect pixels satisfying hypothesis $\overline{B}_{ij}$ is sensitive to the decay length of the marginal Poisson distribution and to the background amplitude, that is recognizable in the distance between the Poisson and the marginal Poisson distributions. Hence, the BSS method allows probabilities to be sensitive to the parameters characterizing the analysed digital astronomical image.

Let us consider plot (b) in Fig. 2 for photon counts in the range (0–10). The background amplitude has a value of 1 count. If the expected mean source intensity on the complete field has a value of 1 count, i.e. $\lambda = 1$ count, 3 photon counts or more in a pixel are classified as a source. The probability of detecting a source increases with increasing counts in a pixel. This is due to the increasing distance of the marginal Poisson likelihood from the Poisson likelihood. If an analyst allows for many bright sources distributed in the field, then the relative number of faint sources is reduced. In fact, when a mean source signal 100 times larger than the background is expected, then 5 photon counts or more in a pixel are needed to identify the event due to the presence of a source. When $\lambda = 100$ counts, 5 photon counts in a pixel reveal a source probability lower than the one obtained when $\lambda = 1$ count. This situation changes for 7 or more photon counts in a pixel.

*3.1.1.2 Inverse-Gamma function prior* Alternatively to the exponential prior, a power-law distribution can be chosen to describe the prior knowledge on the source signal distribution.

We are tempted to claim that any physical situation contains sensible information for a proper (normalizable) prior. We choose a prior pdf that is inspired by the cumulative signal number counts distribution used often in astrophysics for describing the integral flux distribution of cosmological sources, i.e. a power-law function (see Rosati, Borgani & Norman 2002; Brandt & Hasinger 2005 and references therein). The power law cannot be employed as a prior pdf, because the power law is not normalized. We use instead a normalized inverse-Gamma function. It behaves at large counts as the power law, because it is described by a power law with an exponential cut-off.

The prior pdf of the source signal, described by an inverse-Gamma function, is

$$p(s_{ij} \mid \alpha, a) = e^{-(a/s_{ij})} s_{ij}^{-\alpha} \frac{a^{\alpha-1}}{\Gamma(\alpha - 1)}; \quad \alpha > 1, \quad a > 0, \tag{9}$$

with slope $\alpha$ and cut-off parameter $a$. When $a$ has a small positive value, the inverse-Gamma function is dominated by a power-law behaviour.

The parameter $a$ gives rise to a cut-off of faint sources. This parameter has important implications in the estimation of the background. If $a$ is smaller than the background amplitude, the BSS algorithm detects sources of the order of the background. If $a$ is larger than the background amplitude, the BSS algorithm assigns faint sources with intensities lower than $a$ to be background only.

In Fig. 1, equation (9) is drawn for two values of the parameter $\alpha$. For this example the cut-off parameter $a$ has a value of $\sim 0.1$ count. The distributions peak around $a$. The decay of each distribution depends on the value of $\alpha$. When $\alpha$ is large, i.e. for values $\geq 2$, the distribution drops quickly to zero. Instead the distribution drops slowly to zero, when $\alpha$ approaches 1. Hence, small values of $\alpha$ indicate bright sources distributed on the field.

The *marginal Poisson likelihood* for the hypothesis $\overline{B}_{ij}$ is now described by

$$p(d_{ij}|\overline{B}_{ij}, b_{ij}, \alpha, a) = \frac{2}{\Gamma(\alpha - 1)} e^{-b_{ij}} \sum_{k=0}^{d_{ij}} a^{[(k+\alpha-1)/2]}$$

$$\times \frac{b_{ij}^{d_{ij}-k}}{\Gamma(k+1)\Gamma(d_{ij}-k+1)} K_{k-\alpha+1}(2\sqrt{a}),$$

$\qquad\qquad(10)$

where $\alpha > 1$, $a > 0$ and $K_{k-\alpha+1}(2\sqrt{a})$ is the modified Bessel function of order $k - \alpha + 1$.

In order to avoid numerical problems with the Bessel function, the following upward recurrence relation was derived:

$$\widetilde{K}_\nu(z) \equiv \frac{\widetilde{K}_{\nu-2}(z)}{(k-1)k} + \frac{2(\nu-1)}{z\,k}\widetilde{K}_{\nu-1}(z),$$

where $\widetilde{K}_\nu(z) := K_\nu(z)/\Gamma(k+1)$ and $\nu = k - \alpha + 1$. $K_\nu(z)$ is the Bessel function of imaginary argument and it has the property: $K_{-\nu}(z) = K_\nu(z)$.

Figs 2 (d)–(f) show the corresponding parameter study for the inverse-Gamma function prior. The parameter $\alpha$ is chosen to be 1.3, 2.0 and 3.0 and the cut-off parameter $a \sim 0.1$ counts. The decay length of the marginal Poisson distributions (10) are now given by the value of $\alpha$. The decay length decreases with increasing $\alpha$ values.

### 3.1.2 *The likelihood for the mixture model*

The marginal Poisson likelihood pdf will be indicated with $p(d_{ij}|\overline{B}_{ij}, b_{ij}, \gamma)$, where $\gamma$ indicates $\lambda$ or $\alpha$. In the case of the inverse-Gamma function prior pdf, the cut-off parameter $a$ does not appear since the value of this parameter is chosen such that the inverse-Gamma function is dominated by a power-law behaviour.

The likelihood for the mixture model, as written in (5), now reads

$$p(D \mid b, \gamma, \beta) =$$

$$\prod_{ij}[\beta\, p(d_{ij} \mid B_{ij}, b_{ij}) + (1-\beta) \times p(d_{ij} \mid \overline{B}_{ij}, b_{ij}, \gamma)];$$

$$D = \{d_{ij}\}, \quad b = \{b_{ij}\}. \qquad(11)$$

In Fig. 3 we show the effect of the likelihood for the mixture model on the data (semilog plot). The likelihood pdf for the mixture model is drawn for each prior pdf of the source signal employing the background value $b$ and the prior pdf $\beta$. The value chosen for the parameter $\beta$ indicates that 99 per cent of the pixels distributed in the astronomical image are containing only background. The likelihood pdfs are composed by a central peak plus a long tail. The central
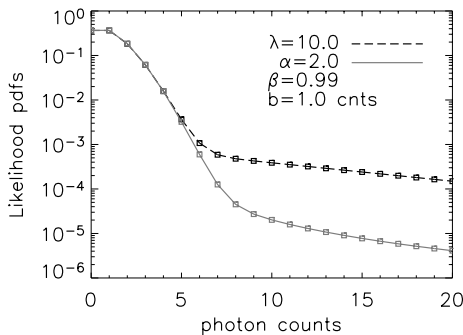


**Figure 3.** Likelihood pdfs for the mixture model using the *exponential prior* (dashed line) and the *inverse-Gamma function prior* (continuous line). The Poisson and the marginal Poisson likelihood pdfs are weighted with $\beta$ and $(1 - \beta)$, respectively.

peak is primarily due to the presence of the Poisson distribution. The long tail is caused by the marginal Poisson distribution. The presence of the long tail is essential in order to reduce the influence of the source signal for background estimation (see Fischer et al. 2000 for more details).

### 3.2 Thin-plate spline

The TPS has been selected for modelling the structures arising in the background rate of a digital astronomical image. It is a type of radial basis function.

The TPS is indicated with $t(\boldsymbol{x})$, where $\boldsymbol{x} = (x, y)$ corresponds to the position on the grid in the detector field. The shape of the interpolating TPS surface fulfils a minimum curvature condition on infinite support.

More specifically, the TPS is a weighted sum of translations of radially symmetric basis functions augmented by a linear term (see Meinguet 1979; Wahba 2006) of the form

$$t(\boldsymbol{x}) = E(\boldsymbol{x}) + \sum_{l=1}^{N_r} \lambda_l f(\boldsymbol{x} - \boldsymbol{x}_l); \quad \boldsymbol{x} \in R^2.$$

$E(\boldsymbol{x}) = c_0 + c_1 x + c_2 y$ is the added plane. $N_r$ is the number of support points (pivots). The weight is characterized by $\lambda_l$. $f(\boldsymbol{x} - \boldsymbol{x}_l)$ is a basis function, a function of real values depending on the distance between the grid points $\boldsymbol{x}$ and the support points $\boldsymbol{x}_l$, such that $|\boldsymbol{x} - \boldsymbol{x}_l| > 0$.

Given the pivots $\boldsymbol{x}_i$ and the amplitude $z_i = z(\boldsymbol{x}_i)$, the TPS satisfies the interpolation conditions

$$t(\boldsymbol{x}_i) = E(\boldsymbol{x}_i) + \sum_{l=1}^{N_r} \lambda_l f(\boldsymbol{x}_i - \boldsymbol{x}_l) = z_i, \quad i = 1, \dots, N$$

and minimizes

$$\|t\|^2 = I[f(x, y)] = \iint_{R^2} \left(f_{xx}^2 + 2f_{xy}^2 + f_{yy}^2\right) \, dx\, dy.$$

$\|t\|^2$ is a measure of energy in the second derivatives of $t$. In other words, given a set of data points, a weighted combination of TPSs centred about each pivot gives the interpolation function that passes through the pivots exactly while minimizing the so-called 'bending energy'. The TPS satisfies the Euler–Lagrange equation and its solution has the form: $f(\boldsymbol{x} - \boldsymbol{x}_l) \simeq r^2 \ln(r^2)$, where $r^2 = (x - x_l)^2 + (y - y_l)^2$. This is a smooth function of two variables defined via Euclidean space distance. In Fig. 4 an example of TPS with one pivot is pictured.

In order to fit the TPS to the data, it is necessary to solve for the weights and the plane's coefficients so that it is possible to interpolate the local TPS's amplitude:

$$t_{ij} = t_{ij}(N_r, \{\boldsymbol{x}_l, z_l, l = 1, \dots, N_r\})$$

which is the background rate. $b_{ij}$ will indicate the local background amplitude, i.e. the multiplication of $t_{ij}$ and the local value of the telescope's exposure time ($\tau$):

$$b_{ij} = t_{ij}\, \tau_{ij}.$$

The TPS interpolant is defined by the coefficients, $c_i$ of the plane $E(\boldsymbol{x})$ and the weights $\lambda_l$ of the basis functions. The solution for the TPS has been evaluated on an infinite support, since no solutions exist on a finite support, where the requirements for this function to be fulfilled are

(i) $t(\boldsymbol{x})$ is two times continuously differentiable,
(ii) $t(\boldsymbol{x})$ takes a particular value $z_i$ at the point $\boldsymbol{x}_i$,

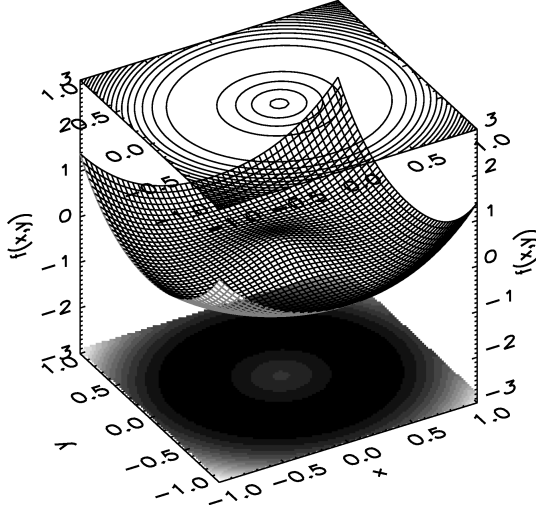**Figure 4.** Example of thin-plate spline. $f(x - x_l) = r^2 \ln(r^2)$ is drawn with one support point centred at the Cartesian origin. The projection of $f(x - x_l)$ on the $(x, y)$ plane is placed below and its contour plot on top of the surface image.

(iii) $I[f(x, y)]$ is finite.

Given the interpolation values $z = (z_1, \ldots, z_{N_r})$, the weights $\lambda_l$ and $c_i$ are searched so that the TPS satisfies

$$t(x_l) = z_l, \quad l = 1, \ldots, N_r,$$

and in order to have a converging integral, the following conditions need to be satisfied:

$$\begin{cases} \sum_{l=1}^{N_r} \lambda_l = 0, \\ \sum_{l=1}^{N_r} \lambda_l x_l = 0, \\ \sum_{l=1}^{N_r} \lambda_l y_l = 0. \end{cases}$$

This means that we have $(N_r - 3)$ conditions on $t(x_l) = z_l$.

The coefficients of the TPS, $\lambda_l$, and the plane, $c_i$, can be found by solving the linear system, that may be written in matrix form as

$$\begin{pmatrix} F & Q \\ Q^T & \mathcal{O} \end{pmatrix} \begin{pmatrix} \lambda \\ c \end{pmatrix} = \begin{pmatrix} z \\ 0 \end{pmatrix},$$

where the matrix components are

$$Q = \begin{pmatrix} 1 & x_1 & y_1 \\ 1 & x_2 & y_2 \\ \vdots & \vdots & \vdots \\ 1 & x_{N_r} & y_{N_r} \end{pmatrix}, \quad \begin{aligned} F_{ij} &= f(x_i - x_j), \\ z &= (z_1, \ldots, z_{N_r})^T, \\ 0 &= (0, 0, 0)^T, \\ \lambda &= (\lambda_1, \ldots, \lambda_{N_r})^T, \\ c &= (c_0, c_1, c_2)^T. \end{aligned}$$

After having solved $(\lambda, c)^T$, the TPS can be evaluated at any point.

The pivots can be equally spaced or can be located in structures arising in the astronomical image. Following the works of Fischer et al. (2000) and von Toussaint & Gori (2007), the present work can be extended employing adaptive splines, i.e. allowing the number of pivots and their positions to vary in accordance with the requirements of the data.

### 3.3 Estimation of the background and its uncertainties

The posterior pdf of the background is, according to Bayes' theorem, proportional to the product of the mixture likelihood pdf, equation (11), and the prior pdf $p(b)$, that is chosen constant for positive values of $b$ and null elsewhere. Its maximum with respect to $b$, $b^*$, gives an estimate of the background map which consists of the TPS combined with the observatory's exposure map. The estimation of the background considers all pixels, i.e. on the complete field, because we tackle the source signal implicitly as outlier.

The posterior pdf for $b$ is given by

$$p(b \mid D) = \int p(b \mid D, z) p(z \mid D) \, \mathrm{d}^{N_r} z$$
$$= \int \delta[b - b(z)] \frac{p(D \mid z) p(z)}{p(D)} \, \mathrm{d}^{N_r} z.$$

This integral is complicated due to the presence of the delta function. This is, however, of minor importance since our interest focuses on the expectation values of some functionals of $b$, say $g(b)$. Therefore,

$$E(g(b) \mid D) = \int g(b) p(b \mid D) \, \mathrm{d}b$$
$$= \int g[b(z)] \frac{p(D \mid z) p(z)}{p(D)} \, \mathrm{d}^{N_r} z$$
$$= \frac{\int g[b(z)] p(D \mid z) p(z) \, \mathrm{d}^{N_r} z}{\int p(D \mid z) p(z) \, \mathrm{d}^{N_r} z}. \tag{12}$$

Assuming the maximum of $p(D \mid z)\, p(z)$ is well determined we can apply the Laplace approximation:

$$p(D \mid z) p(z) \simeq p(D \mid z^*) p(z^*) \exp\left\{-\frac{1}{2} \Delta z^T H \Delta z\right\}, \tag{13}$$

that means we approximate the integral function by a Gaussian at the maximum $z^*$ and we compute the volume under that Gaussian. The covariance of the fitted Gaussian is determined by the Hessian matrix, as given by (13), where $\Delta z = z - z^*$ and $H_{ij} := -\{\partial^2 \ln[p(D \mid z) p(z)]/(\partial z_i \, \partial z_j)\}$ is element $\{ij\}$ of the Hessian matrix. This approximation is the second-order Taylor expansion of the posterior pdf around the optimized pivots amplitude's values. For more details see O'Hagan & Forster (2004).

Then equation (12) becomes

$$E(g(b) \mid D) = \frac{\int g[b(z)] \exp\left\{-(1/2)\Delta z^T H \Delta z\right\} \, \mathrm{d}^{N_r} z}{(2\pi)^{N_r/2} (\det H)^{-(1/2)}}.$$

Therefore, the posterior mean of $b$ is

$$E(b_{ij} \mid D) = \frac{\sqrt{\det H}}{(2\pi)^{N_r/2}} \int b_{ij}(z) \exp\left\{-\frac{1}{2}\Delta z^T H \Delta z\right\} \mathrm{d}^{N_r} z$$
$$= T_{ij}^T z^* = \langle b_{ij} \rangle,$$

where $b_{ij}(z) = T_{ij}^T \cdot z$, and the variance is

$$E(\Delta b_{ij} \Delta b_{lk} \mid D) = \frac{\sqrt{\det H}}{(2\pi)^{N_r/2}} \int [b_{ij}(z) - \langle b_{ij} \rangle]$$
$$\times [b_{lk}(z) - \langle b_{lk} \rangle] \exp\left\{-\frac{1}{2}\Delta z^T H \Delta z\right\} \mathrm{d}^{N_r} z$$
$$= T_{ij}^T H^{-1} T_{lk}. \tag{14}$$

The $1\sigma$ error on the estimated background function is therefore calculated by the square root of equation (14).

### 3.4 Determining the hyperparameters

The two hyperparameters $\gamma$ and $\beta$ have so far been assumed to be fixed. However, these parameters can be appropriately estimated from the data.

Within the framework of BPT the hyperparameters (nuisance parameters) $\gamma$ and $\beta$ have to be marginalized.

Alternatively, and not quite rigorous in the Bayesian sense, the hyperparameters can be estimated from the marginal posterior pdf, where the background and source parameters are integrated out,

$$\max_{\beta, \gamma} p(\beta, \gamma \mid D) \to \beta^*, \gamma^*.$$

Hence, the estimate of the hyperparameters is the maximum of their joint posterior.

The basic idea is to use BPT to determine the hyperparameters explicitly, i.e. from the data. This requires the posterior pdf of $\gamma$ and $\beta$. Bayes' theorem gives

$$p(\gamma, \beta \mid D) = \frac{p(D \mid \gamma, \beta) p(\gamma) p(\beta)}{p(D)}. \tag{15}$$

The prior pdfs of the hyperparameters are independent because the hyperparameters are logically independent. These prior pdfs are chosen uninformative, because of our lack of knowledge on these parameters. The prior pdf for $\beta$ is chosen to be constant in [0,1]. Since $\gamma$ is a scale parameter, the appropriate prior distribution is Jeffrey's prior: $p(\gamma) \sim 1/\gamma$. Equation (15) can be written as follows:

$$p(\gamma, \beta \mid D) \propto p(D \mid \gamma, \beta) p(\gamma) = p(\gamma) \int p(D \mid z, \gamma, \beta) p(z) \, \mathrm{d}z. \tag{16}$$

Assuming the maximum of $p(D \mid z, \gamma, \beta) p(z)$ is well determined, we can apply the Laplace approximation

$$p(D \mid z, \gamma, \beta) p(z) \simeq p(D \mid z^*, \gamma, \beta) p(z^*) \exp\left\{-\frac{1}{2} \Delta z^\mathrm{T} H \Delta z\right\},$$

where $\Delta z = z - z^*$, $z^*$ corresponds to the maximum value of the integrand in (16), and $H_{ij} := -\{\partial^2 \ln[p(D \mid z, \gamma, \beta) p(z)]/(\partial z_i \partial z_j)\}$ is element $\{i\,j\}$ of the Hessian matrix. Considering $\dim(z) = N_\mathrm{r}$, where $N_\mathrm{r}$ is the number of support points, equation (16) can be written as follows:

$$p(\gamma, \beta \mid D) = p(\gamma) p(D \mid z^*, \gamma, \beta) p(z^*) \frac{(2\pi)^{N_\mathrm{r}/2}}{(\det H)^{1/2}},$$

$p(z^*)$ is chosen to be constant. The last term corresponds to the volume of the posterior pdf of $\gamma$ and $\beta$ for each $\gamma$, $\beta$ estimates.

## 3.5 Probability of hypothesis $\overline{B}$

In principle, the probability of detecting source signal in addition to the background should be derived marginalizing over the background coefficients and the hyperparameters. Following the works of von der Linden et al. (1999) and Fischer et al. (2000), the multidimensional integral, arising from the marginalization, can be approximated at the optimal values found of the background coefficients and the hyperparameters.

Equation (6) is approximated with

$$p(\overline{B}_{ij} \mid d_{ij}) \approx$$
$$\frac{1}{1 + [\beta/(1-\beta)] \left[ p\left(d_{ij} \mid B_{ij}, b_{ij}^*\right) / p\left(d_{ij} \mid \overline{B}_{ij}, b_{ij}^*, \gamma\right) \right]} = P_\mathrm{source}, \tag{17}$$

where $b^* = \{b_{ij}^*\}$ is the estimated background amplitude, as explained in Section 3.3. SPMs are estimated employing this formula.

The BSS method does not incorporate the shape of the PSF. When the PSF full width at half-maximum (FWHM) is smaller than the image pixel size, then one pixel contains all the photons coming from a point-like source. Otherwise point-like sources are detected on pixel cells as large as the PSF FWHM. Extended objects are detected in pixel cells large enough that the source size is completely included. The pixel cell must be larger than the PSF FWHM and it can exhibit any shape.

Equation (17) shows that the source probability strictly depends on the ratio between the Poisson likelihood, $p(d_{ij} \mid B_{ij}, b_{ij})$, and the marginal Poisson likelihood, $p(d_{ij} \mid \overline{B}_{ij}, b_{ij}, \gamma)$ (Bayes factor). Bayes factors offer a way of evaluating evidence in favour of competing models.

Fig. 5 shows the effect of the mixture model technique on the probability of having source contribution in pixels and pixel cells for the exponential and the inverse-Gamma function prior pdfs. For the parametric studies, the parameter $\beta$ is chosen to be 0.5. This non-committal value of $\beta$ arises if each pixel (or pixel cell) is equally likely to contain source signal contribution or background only. $P_\mathrm{source}$ depends on the likelihood for the mixture model, which
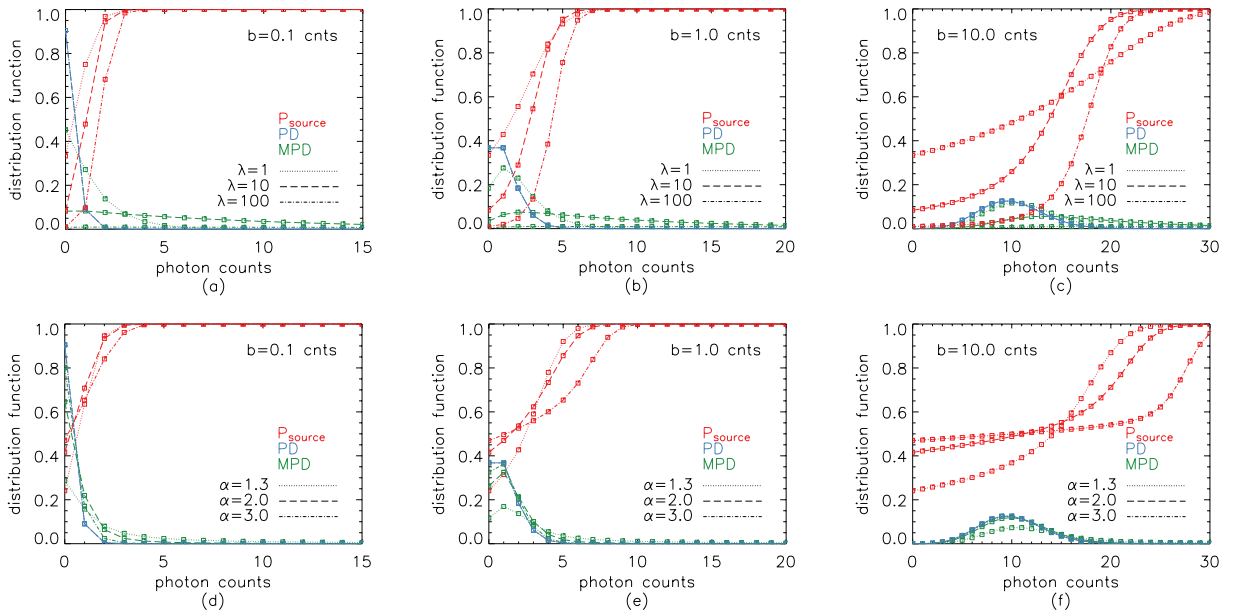


**Figure 5.** Source probability ($P_\mathrm{source}$), PD and MPD versus photon counts as given by equations (17), (3) and (8) for the *exponential prior* pdf, panels (a)–(c); equations (17), (3) and (10) for the *inverse-Gamma function prior* pdf, panels (d)–(f).

**Table 1.** Interpretation of source probability values.

| $P_{source}$ (per cent) | <50 | 50 | 90 | 99 | 99.9 |
|---|---|---|---|---|---|
| Interpretation | Backg. only | Indif. | Weak | Strong | Very strong |

is the weighted sum of the Poisson distribution and the marginal Poisson distribution. For photon counts of about the mean background intensity, $P_{source}$ is small. $P_{source}$ increases with increasing photon counts due to the presence of the long tail in the marginal likelihood. This allows efficient separation of the source signal from the background.

In panels (a)–(c), the distribution function of $P_{source}$, the Poisson pdf (PD) and the marginal Poisson pdf (MPD) are drawn using the exponential prior (see also Figs 1 and 2). In the case of fields with bright sources ($\lambda > 10$ times the background intensity), $P_{source}$ is nearly zero for photon counts less than or equal to the mean background intensity. $P_{source}$ increases rapidly with increasing photon counts. In the case of fields where the mean source intensity is similar to the mean background intensity, pixels containing photon counts close to the mean background intensity have probabilities about 50 per cent. In these cases, $P_{source}$ increases slowly with increasing photon counts, because the two Poisson distributions are similar. In the case of fields dominated by large background signal ($\lambda <$ mean background amplitude), $P_{source}$ increases very slowly with increasing photon counts. In this case, the decay of the marginal Poisson distribution follows closely the decay of the Poisson distribution (e.g. for $b = 10$ counts and $\lambda = 1$ count).

In Fig. 5, panels (d)–(f), the distribution functions are shown using the inverse-Gamma function prior (see also Figs 1 and 2). The steepness of the slope depends on the parameter $\alpha$ (Fig. 1). The source probability curve increases faster at decreasing $\alpha$ values, because small $\alpha$ values indicate bright sources distributed in the field. In panels (e) and (f), $P_{source}$ provides values close to 50 per cent at low numbers of photon counts. This effect addresses the cut-off parameter $a$. In fact, in these plots the cut-off parameter $a$ is smaller than the background amplitude. The situation is different in the simulations with small background amplitude (panel d), where the source probabilities decrease below 50 per cent at low numbers of photon counts. In these simulations the cut-off parameter $a$ is chosen larger than the mean background amplitude. Faint sources with intensities lower than $a$ are described to be background.

The interpretations of the probability of having source contributions in pixels and pixel cells are shown in Table 1. Source probabilities <50 per cent indicates the detection of background only. $P_{source}$ is indifferent at values of 50 per cent. In both cases, $P_{source}$ might contain sources but they cannot be distinguished from the background due to statistical fluctuations. Source probability values ≫50 per cent indicate source detections. False sources due to statistical fluctuations may occur especially for values <99 per cent. For more details about the interpretations provided in Table 1, see Jeffreys (1961) and Kass & Raftery (1995).

### 3.5.1 Statistical combination of SPMs at different energy bands

An astronomical image is usually given in various energy bands. SPMs, obtained with (17), acquired at different energy bands can be combined statistically. The probability of detecting source signal in addition to the background for the combined energy bands $\{k\}$

is

$$p(\overline{B}_{ij} \mid d_{ij})_{comb} = 1 - \prod_{k=1}^{n}[1 - p(\overline{B}_{ij} \mid d_{ij})_k], \qquad (18)$$

where $n$ corresponds to the effective energy band.

Equation (18) allows one to provide conclusive posterior pdfs for the detected sources from combined energy bands. It results, as expected, that if an object is detected in multiple bands, the resulting $p(\overline{B}_{ij} \mid d_{ij})_{comb}$ is larger than the source probability obtained analysing a single band. An application of this technique is shown in Section 8.1.1. This analysis can be extended to study crowded fields or blends by investigating source colours.

## 4 SOURCE CHARACTERIZATION

Following the estimation of the background and the identification of sources, the sources can be parametrized. SPMs at different resolutions are investigated first. Sources are catalogued with the largest source probability reached in one of the SPMs. Local regions are chosen around the detected sources. The region size is determined by the correlation length where the maximum of the source probability is reached.

Although any suitable source shape can be used, we model the sources by a two-dimensional Gaussian. The data belonging to a source detection area 'k' are given by

$$D_{ij} = b_{ij} + G_{ij} \qquad \forall\{ij\} \in \{k\}. \qquad (19)$$

$D_{ij}$ are the modelled photon counts in a pixel $\{ij\}$ spoiled with the background counts $b_{ij}$. $G_{ij}$ is the function which describes the photon counts distribution of the detected source:

$$G_{ij} = \frac{I}{2\pi\sigma_x\sigma_y\sqrt{1-\rho^2}} \exp\left\{ -\frac{1}{2(1-\rho^2)} \left[ \left(\frac{x_{ij}-x_s}{\sigma_x}\right)^2 \right.\right.$$
$$\left.\left. + \left(\frac{y_{ij}-y_s}{\sigma_y}\right)^2 - 2\rho\left(\frac{x_{ij}-x_s}{\sigma_x}\right)\left(\frac{y_{ij}-y_s}{\sigma_y}\right) \right] \right\},$$

where $I$ is the intensity of the source, i.e. the net source counts, $\sigma_x$, $\sigma_y$ and $\rho$ provide the source shape and $x_s$, $y_s$ is the source pixel position on the image.

Position, intensity and source shape are provided maximizing the likelihood function assuming constant priors for all parameters:

$$p(x_s, y_s, I, \sigma_x, \sigma_y, \rho|b, d) \propto \prod_{ij} \frac{D_{ij}^{d_{ij}}}{d_{ij}!} \exp\{-D_{ij}\}$$
$$\forall\{ij\} \in \{k\}, \qquad (20)$$

where $d_{ij}$ are the photon counts detected on the image.

According to (19) and (20) the source fitting is executed on the sources for given background. This is reasonable since the uncertainty of the estimated background is small. No explicit background subtraction from the photon counts is needed for estimating the source parameters.

Source position and extensions are converted from detector space to sky space. Source fluxes are provided straightforwardly.

The rms uncertainties of the source parameters are estimated from the Hessian matrix, where $H_{ij} := -\{\partial^2 \ln[p(D \mid \xi)p(\xi)]/(\partial\xi_i \partial\xi_j)\}$ is element $\{ij\}$ of the Hessian matrix and $\xi$ indicates the source parameters. The square root of the diagonal elements of the inverse of the Hessian matrix provides the $1\sigma$ errors on the estimated parameters.

The output catalogue includes source positions, source counts, source count rates, background counts, source shapes and their

errors. The source probability and the source detection's resolution are incorporated.

Source characterization can be extended with model selection. With the Bayesian model selection technique, the most suitable model describing the photon count profile of the detected sources can be found. The models to be employed are, for instance, Gaussian profile, King profile (Cavaliere & Fusco-Femiano 1978), de Vaucouleurs model and Hubble model. Such an extension to the actual method would allow an improvement in the estimation of the shape parameters of faint and extended sources.

# 5 RELIABILITY OF THE DETECTIONS

There are several methods for reducing the number of false positives, one is to use $p$ values from statistical significance tests (Linnemann 2003). $p$ values are used to a great extent in many fields of science. Unfortunately, they are commonly misinterpreted. Researches on $p$ values (e.g. Berger & Sellke 1987) showed that $p$ values can be a highly misleading measure of evidence.

In Section 5.1 we provide the definition of $p$ values. In Section 5.2, we express our general view on how this problem can be tackled with BPT. The commonly used measure of statistical significance with Poisson $p$ values is introduced in Section 5.3. In Section 5.4 simulations are used for comparing the Poisson $p$ values with the Bayesian probabilities.

## 5.1 $p$ values

In hypothesis testing one is interested in making inferences about the truth of some hypothesis $H_0$, given a set of random variables $X : X \sim f(x)$, where $f(x)$ is a continuous density and $x$ is the actual observed values. A statistic $T(X)$ is chosen to investigate compatibility of the model with the observed data $x$, with large values of $T$ indicating less compatibility (Sellke, Bayarri & Berger 2001). The $p$ value is then defined as

$$p = Pr(T(X) \geq T(x)|H_0).$$

The significance level of a test is the maximum allowed probability, assuming $H_0$, that the statistic would be observed. The $p$ value is compared to the significance level. If the $p$ value is smaller than or equal to the significance level then $H_0$ is rejected. The significance level is an arbitrary number between 0 and 1, depending on the scientific field one is working in. However, classically a significance level of 0.05 is accepted. Unfortunately, the significance level of 0.05 does not indicate a particular strong evidence against $H_0$, since it just claims an even chance.

An extensive literature dealing with misinterpretations about $p$ values exists, see e.g. Berger & Delampady (1987), Berger & Sellke (1987), Berger & Berry (1988), Delampady & Berger (1990), Loredo (1990, 1992), Kass & Raftery (1995), Sellke et al. (2001), Gregory (2005) and references therein.

## 5.2 The Bayesian viewpoint

Since the state of knowledge is always incomplete, a hypothesis can never be proved false or true. One can only compute the probability of two or more competing hypotheses (or models) on the basis of the only data available, see e.g. Gregory (2005).

The Bayesian approach to hypothesis testing is conceptually straightforward. Prior probabilities are assigned to all unknown hypotheses. Probability theory is then used to compute the posterior probabilities of the hypotheses given the observed data (Berger

1997). This is in contrast to standard significance testing which does not provide such interpretation. In fact, in the classic approach the truth of a hypothesis can be only inferred indirectly.

Finally, it is important to underline that the observed data and parameters describing the hypotheses are subject to uncertainties which have to be estimated and encoded in probability distributions. With BPT there is no need to distinguish between statistical (or random) and systematic uncertainties. Both kinds of uncertainties are treated as lack of knowledge. For more on the subject see Fischer et al. (2003).

## 5.3 Significance testing with $p$ values

Several measures of statistical significance with $p$ values have been developed in astrophysics. A critical comparison and discussion about methods for measuring the significance of a particular observation can be found in Linnemann (2003). Following Linnemann, our attention is focused on the Poisson probability $p$ value:

$$p_P = P(\geq d|b) = \sum_{j=d}^{\infty} \frac{e^{-b} b^j}{j!}. \tag{21}$$

$p_P$ is the probability of finding $d$ or more (random) events under a Poisson distribution with an expected number of events given by $b$. Linnemann remarks that Poisson probability $p$ value estimates lead to overestimates of the significance since the uncertainties on the background are ignored.

## 5.4 Comparing threshold settings for source reliability

In order to restrain the rates of false source detections per field, a threshold on probabilities is commonly set according to the goal of a specific research. For instance, Freeman et al. (2002) have chosen an upper limit of one spurious detection per analysed *Chandra* field. This value corresponds to a false-positive probability threshold of $10^{-7}$. The method developed by Freeman et al. (2002) is a wavelet-based source detection algorithm (WAVDETECT). For the *XMM–Newton* serendipitous source catalogue, Watson et al. (2003) have chosen a detection likelihood $L = 10$, corresponding to $\approx 4\sigma$. $L$ is given by $-\ln(1 - P)$, where $P$ is the probability of source detection obtained by a maximum likelihood method (Cruddace, Hasinger & Schmitt 1988). The selected likelihood threshold corresponds to the detection of <1 spurious source per field. In any systematic investigation to source detection, the threshold level is a trade-off between the detection power and false detections rate.

Following this idea, the Poisson probability $p$ value (21) is compared to the Bayesian source probability (17). Fig. 6 compares the two statistics. Panel (a) shows the relation between $p_P$ and $(1 - P_{source})$ for varying background amplitudes and source intensities. Panel (b) displays the same data but with fixed background value and varying source intensities. These results are obtained employing the exponential prior. A more detailed study, including the inverse-Gamma function prior, can be found in Guglielmetti (in preparation). The squares on each plot indicate the photon counts $d$ chosen for calculating (21). On the abscissa, the background probability is calculated as the complementary source probability provided by the Bayesian method. The value close to unity corresponds to a source probability, $P_{source}$, which goes to zero, instead a value of 0.1 corresponds to 90 per cent source probability and 0.01 to 99 per cent source probability.

Each plot shows a general tendency. For a given count number $d$, $P_{source}$ and $(1 - p_P)$ increase with decreasing background intensity.
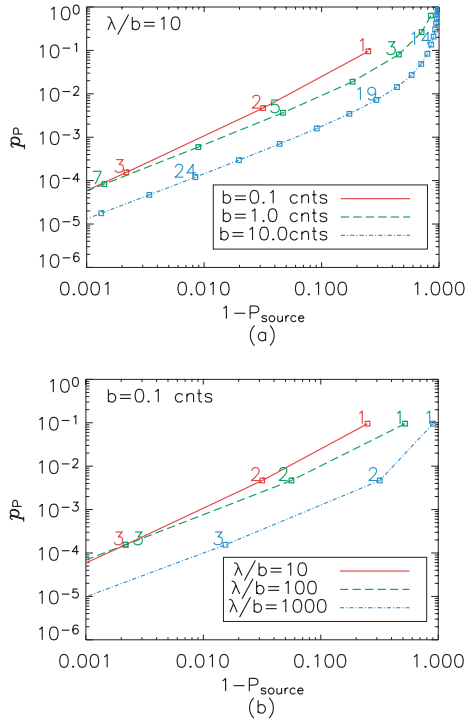
**Figure 6.** Classic hypothesis testing versus Bayesian approach.

**Table 2.** Bayesian source probability ($P_{source}$) versus Poisson $p$ value ($p_P$).

| $b$ (counts) | $\lambda$ (counts) | $d$ (counts) | $P_{src}$ | $1 - p_P$ | $1 - P_{src}$ | $p_P$ |
|---|---|---|---|---|---|---|
| 0.1 | 1.0 | 2 | 0.97 | 0.995 | 0.03 | 0.005 |
| 1.0 | 10.0 | 2 | 0.29 | 0.74 | 0.71 | 0.26 |
| 10.0 | 100.0 | 2 | 0.01 | 0.0005 | 0.99 | 0.9995 |

Note. This example shows the variation of $P_{source}$, here indicated with $P_{src}$, and $p_P$ for detecting 2 photon counts in a pixel at three background levels. $P_{source}$ represents the source probability of detecting 2 photon counts ($d$) in a pixel according to the Bayesian technique. $(1 - p_P)$ is the cdf. It provides the probability of detecting 1 photon count or less in a pixel according to Poisson statistics. $(1 - P_{source})$ is the background probability estimated with the Bayesian method. $p_P$ provides the probability of detecting 2 photon counts or more in a pixel according to Poisson statistics.

However, $P_{source}$ is more conservative. This is due to the dependency of $P_{source}$ not only on the mean background intensity but also on the source intensity distribution. This dependency is expressed by the likelihood for the mixture model (5), that plays a central role for the estimation of the source probability (17). An example of the different interpretations of source detection employing the two statistics is provided in Table 2.

In Fig. 7, $P_{source}$ for a given number of photon counts in a pixel versus $\lambda/b$, the ratio between the mean source intensity and the background intensity, is drawn for a fixed background value. The abscissa is drawn on a logarithmic scale. For a given number of photon counts, the value of $P_{source}$ varies with the source intensities expected in the astronomical image and with the background amplitude. For 2 photon counts, $P_{source}$ reaches a maximum where the mean source intensity in the field has values in the range (1–5) counts. In this part of the curve, 2 photon counts in a pixel are discriminated best from the background. Away from this range, the source probability decreases. For small $\lambda/b$ values, $P_{source}$ approaches 0.5 be-
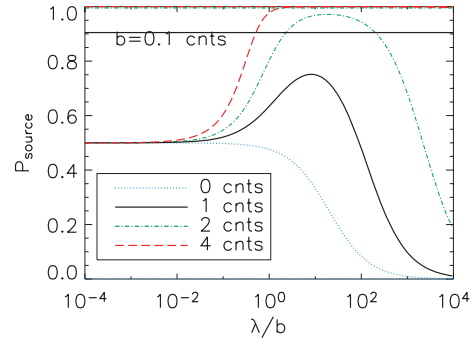


**Figure 7.** Dependency of the Bayesian source probability on the source intensities distributed on a field.

cause source and background cannot be distinguished. For large $\lambda/b$ values, $P_{source}$ decreases since more sources with large intensities are expected relative to small intensities. Therefore, a signal with 2 counts is assigned to be background photons only.

$(1 - p_P)$ is calculated for the same values of background and photon counts as for $P_{source}$. $(1 - p_P)$ is constant, since it does not depend on the source intensities expected in the field. Its value for 2 photon counts, as seen in Table 2, is larger than the maximum of $P_{source}$. In general, $(1 - p_P)$ is larger than $P_{source}$ for values of photon counts larger than the mean background intensity. If the values of the photon counts are lower than or equal to the mean background intensity, $(1 - p_P)$ is lower than the maximum of $P_{source}$.

The comparison shows that it is not possible to calibrate $p_P$ with $P_{source}$ because of the intrinsic difference in the nature of the two statistics. In fact, Poisson $p$ values do not provide an interpretation about background or sources and do not include uncertainties on the background. The Bayesian method, instead, gives information about background and sources and their uncertainties.

The comparison between the two statistics reveals that slightly different answers are arising for the two priors of the source signal. When the exponential prior is employed, fields with large intensities are less penalized by false positives caused by random Poisson noise than fields with source signal very close to the background amplitude. When the inverse-Gamma function prior is used, false positives detections depend on the cut-off parameter $a$. This is because the cut-off parameter has an effect on faint sources. The same behaviour is expected on false positives in source detection. The exponential prior, instead, does not exclude small source intensities. Note that the choice of the source signal prior pdf is crucial for source detection. For a reliable analysis the source signal prior chosen has to be as close as possible to the true one.

## 6  SIMULATED DATA

Artificial data are used for performance assessment of the BSS technique. Three simulations are analysed utilizing the exponential and the inverse-Gamma function prior pdfs of the source signal. The data sets, described in Section 6.1, are meant to test the capabilities of the BSS method at varying background values. The idea is to cover different cases one encounters while surveying different sky regions or employing instruments of new and old generations. In Section 6.2 we review the outcome of our analysis on the three simulated data sets. Comments are given for each feature of the developed technique. In Section 6.3 we provide a summary on the outcome of our analysis.

### 6.1 Simulations set-up

Three sets of simulated fields composed of 100 sources modelled on a constant background with added Poisson noise are generated. Groups of 10 sources are characterized by the same number of photon counts but with different sizes. A logarithmic increment in photon counts per group is chosen ranging from 1 to 512. The shape of each source is characterized by a two-dimensional circular Gaussian. The source extensions, given by the Gaussian standard deviation, increase from 0.5 to 5.0 pixels in steps of 0.5. Sources are located equidistantly on a grid of $500 \times 500$ pixels. Initially, the simulated sources are located on the grid such that the source intensities increase on the abscissa, while the source extensions increase on the ordinate. Subsequently, the 100 sources are randomly permuted on the field. A background is added on each simulated field with values of 0.1, 1 and 10 counts, respectively. We assume a constant exposure.

In Fig. 8, we show one out of three data sets: the simulated data with small background. Image (a) represents the simulated data with added Poisson noise. The image indicated with (b) is the simulated data without Poisson noise. It is placed for comparison. The simulated data sets (a) and (b) are scaled in the range (0–3) photon counts pixel$^{-1}$ in order to enhance faint sources. The original scale of the simulated data with Poisson noise is (0–317) photon counts pixel$^{-1}$. The simulated data without Poisson noise show counts pixel$^{-1}$ in the range (0.1–326.0).

The images representing the other two data sets for $b = 1$ and 10 counts are similar to the one shown in Fig. 8. In these data sets, the number of sources to be separated from the background decreases with increasing background intensity.

The cut-off parameter $a$ is chosen to be 0.14 counts in the three simulated data sets. This is to show the effect of $a$ when the background is smaller or larger than $a$.
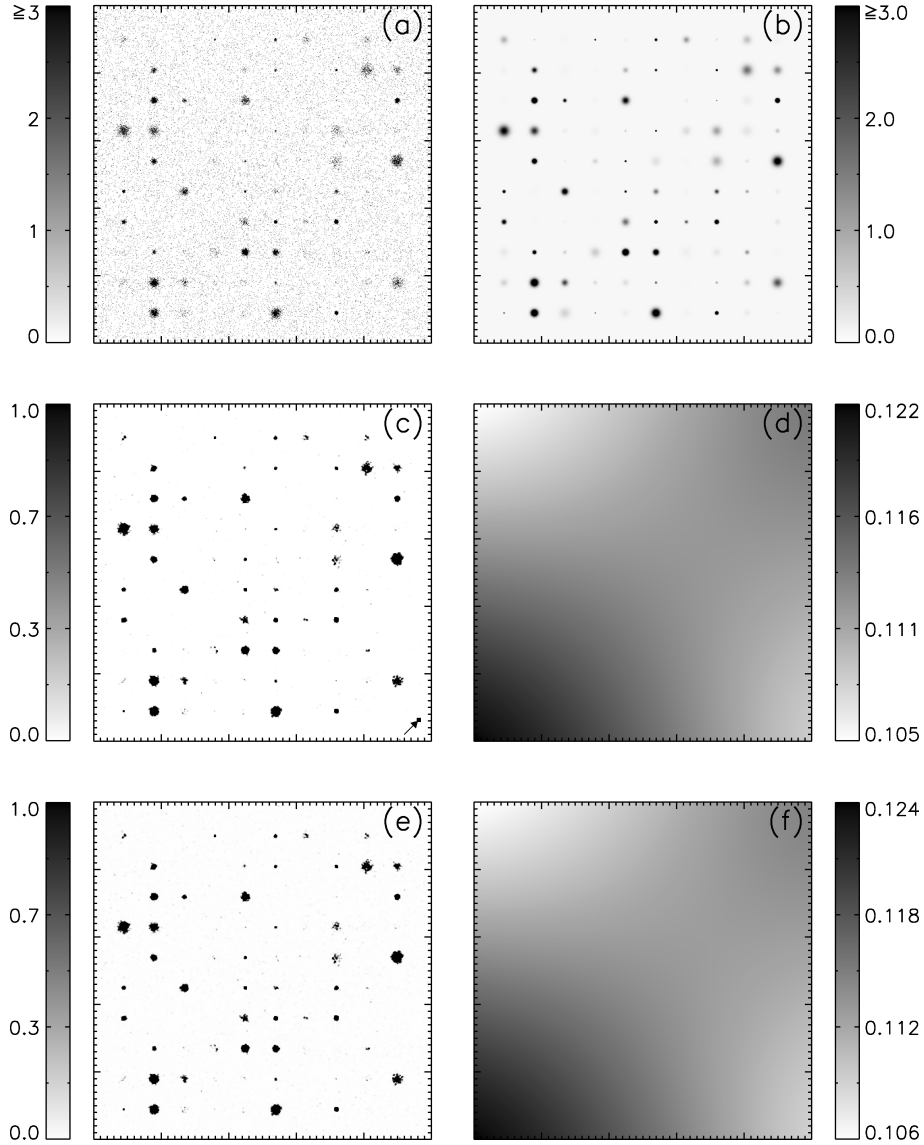


**Figure 8.** Panels (a) and (b): simulated data with small background: image with Poisson noise and image without Poisson noise, respectively. Panels (c) and (d): results with *exponential prior* pdf: SPM with 3-pixel resolution and background map, respectively. Panels (e) and (f): results with *inverse-Gamma function prior* pdf.

## 6.2 Results

### 6.2.1 Background estimation

For the background modelling, only four pivots located at the field's corners are used. This choice is driven by the presence of a constant background. An optimization routine is used for maximizing the likelihood for the mixture model (5). The solution of the optimization routine is the pivots amplitude's estimates from which the background is calculated.

The three set-ups are designed such that half of the 100 simulated sources are characterized by $\leq 16$ photon counts. Some of these simulated sources are too faint for being detected. These sources may contribute to the background model.

In Fig. 8, the estimated background maps are displayed when employing the exponential prior pdf (image d) and the inverse-Gamma function prior pdf (image f) for the simulated data with small background.

The two images show that the background intensity decreases slightly toward the upper left- and lower right-hand corners of about 5 per cent. The same trend is seen also in the estimated backgrounds with intermediate and large values. Evidently, this effect is not introduced by the prior over the signal. Furthermore, it is not introduced by the selected pivots positions. If that were the case, then the same magnitude is expected at each image corner. Instead, this is an overall effect induced by the simulated sources. All simulated sources are randomly permuted. In the upper left- and lower right-hand corners are located numerous faint sources. In the lower left-hand corner many bright sources are clustered. The increment in the background intensity is due to the statistical distribution of the sources. This explains why the same trend in background intensities is seen in all background models.

When employing the exponential prior pdf, the estimated background intensities are in agreement with the simulated background amplitudes. In the case of the inverse-Gamma function prior pdf, the estimated backgrounds are sensitive to the cut-off parameter $a$. When $a$ is set larger than the mean background (i.e. simulated data with small background), the background is overestimated. The overestimated background is due to the presence of source signal below the cut-off parameter. Hence, no source intensities below 0.14 counts are allowed. It results that the estimated background is 40 per cent larger than the simulated one. For simulated data with intermediate background, the cut-off parameter $a$ is fixed to a value lower than the simulated background. The background is underestimated by only $\sim$1 per cent with respect to the simulated one. For simulated data with large background, the cut-off parameter $a$ is much lower than the simulated mean background value. The estimated background is in agreement with the simulated one.

The background uncertainties are quite small compared with the background itself, on the order of few a per cent. This effect holds because the background is estimated on the full field. However, the errors increase where the estimates deviate from the simulated background. In addition, when applying the inverse-Gamma function prior pdf, the errors are larger than those found utilizing the exponential prior pdf.

### 6.2.2 Hyperparameter estimation

In Fig. 9 the contour plot in ($\lambda$, $\beta$) parameter space for the joint probability distribution is shown for the hyperparameters evaluated from the simulated data with small background. The contour levels indicate the credible regions. The values of the estimated hyperpa-
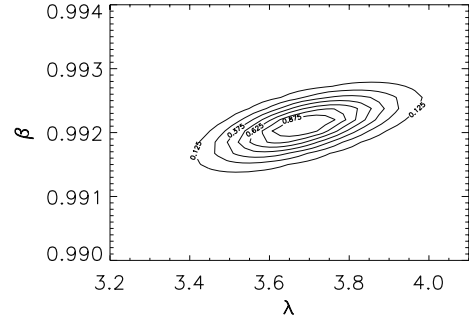


**Figure 9.** Contour plot of the posterior pdf for the hyperparameters, $p(\lambda, \beta|D)$, estimated from the simulated field with small background using the *exponential prior* pdf.

rameters are $\beta = (99.2 \pm 0.03)$ per cent, $\lambda = (3.68 \pm 0.1)$ counts. The estimated $\beta$ value provides the information that only 0.8 per cent of the pixels in the field contains sources. A similar answer is found with the other simulated data: the $\beta$ value increases slightly at increasing background amplitudes. $\lambda$, instead, provides the mean source intensity in the field. The estimated value of $\lambda$ increases with increasing background amplitudes because small intensities are assigned to be background.

When employing the inverse-Gamma function prior pdf, the hyperparameter $\alpha$ is found with the smaller value in the simulated data with small background. The largest value of $\alpha$ is found in the simulated data with intermediate background. Large values of $\alpha$ indicates that more faint sources and less bright sources are expected in the field (Fig. 1). These results do not contradict our expectations on the hyperparameter estimates, since the cut-off parameter selects the source signal distribution at the faint end.

### 6.2.3 The components of the mixture model

In Fig. 10, the Poisson and the marginal Poisson distributions multiplied with their prior knowledge on the model are plotted over the normalized histogram of each simulated data set. The likelihoods are drawn for the exponential and inverse-Gamma function prior pdfs. The values of the estimated hyperparameters are shown in each image.

The exponential prior pdf is plotted over the histogram with a continuous line. The inverse-Gamma function prior pdf, instead, is plotted with a dashed line. The simulated data are neither distributed exponentially nor as an inverse-Gamma function. Hence, the prior pdfs of the source signal are not expected to fit the data exactly.

The marginal Poisson distribution weighted with $(1 - \beta)$ is drawn with a dash–dot line when employing the exponential prior and with long dashes line in the case of the inverse-Gamma function prior. The Poisson distribution (dotted line) is weighted with $\beta$ for the exponential and the inverse-Gamma function prior pdfs.

The intersection between the Poisson pdf and the marginal Poisson pdf indicates the source detection sensitivity. When employing the exponential prior in the simulated data with small background (panel a), the exponential prior enables the detection of fainter sources than the inverse-Gamma function prior. This is expected since the cut-off parameter occurs at a value larger than the simulated mean background. Considering the simulated data with intermediate background (panel b), the detection is more sensitive to faint sources when employing the inverse-Gamma function prior compared to the exponential prior. In fact, the cut-off parameter allows to describe as source signal part of the simulated background
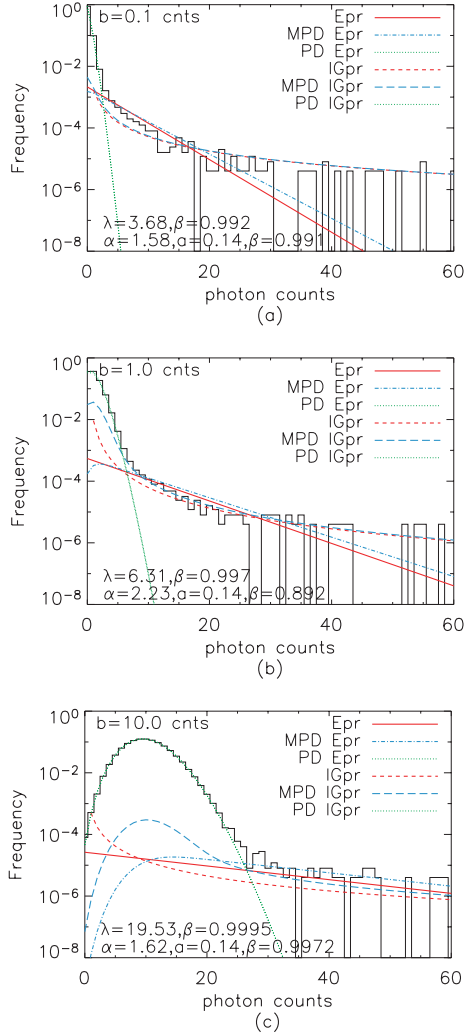
**Figure 10.** Normalized histograms of the simulated data with small (panel a), intermediate (panel b) and large (panel c) backgrounds are displayed. The exponential prior (Epr), inverse-Gamma function prior (IGpr) and related MPD and PD are plotted over the data. The ordinates are in logarithmic scale.

amplitude. For the simulated data with large background (panel c), the same sensitivity in source detection is expected when employing the two priors over the signal distribution.

### 6.2.4 Source probability maps

The box filter method with cell shape of a circle is used in the three simulations for the multiresolution analysis. Examples of SPMs are shown in Fig. 8 for the simulated data with small background. Images (c) and (e) are obtained employing the exponential and the inverse-Gamma function prior pdfs, respectively. These images represent the probability of having source contributions in pixel cells with a resolution of 1.5 pixels. At this resolution a pixel cell is composed of 9 pixels. A pixel cell with a correlation radius of 1.5 pixels is drawn in the lower right-hand corner of image (c) (Fig. 8). It is indicated with an arrow.

The multiresolution technique provides an analysis of source probabilities variation and of source features of the detected sources. In Fig. 11, we display the photon count image and the SPMs zoomed in a bright extended source. This source is detected with the largest

source probability ($\sim$1) at 2.5-pixel resolution. At this resolution the source is detected as one unique object, as given by the simulation. At larger resolutions, instead, the source is dissociated in small parts as seen in the photon count image. This indicates that the source counts are not distributed uniformly. In an astronomical observation, more information is required in order to understand the nature of such sources. Secondly, the maximum in source probability is reached at a correlation length that is smaller than the source size. This is due to the source brightness relatively to the small background value. Within the range of resolutions studied, the source probability is constant at correlation lengths larger than 2.5 pixels.

This example shows that the multiresolution technique combined with the BSS method is particularly appropriate for the search of extended and non-symmetrical sources.

### 6.2.5 Comparison between estimated and simulated source parameters

Source parameters and their uncertainties are derived as described in Section 4. Sources are catalogued when a probability larger than 50 per cent is reached at least in one of the SPMs. This threshold is chosen within these simulated data sets in order to clarify the interpretations provided in Table 1.

The parameters of bright sources are precisely estimated. In Fig. 11 we give an example of detection of a bright extended source employing SPMs in the multiresolution technique. The true parameters of this source are 128 photon counts, $(\sigma_x, \sigma_y) = (5, 5)$, $(x, y) = (360, 270)$. The estimated parameters of this source are $(129.79 \pm 23.70)$ net source counts, $(\sigma_x, \sigma_y) = (4.92 \pm 0.67, 4.96 \pm 0.71)$ pixels, $(x, y) = (359.57 \pm 0.92, 269.29 \pm 0.98)$ pixels. Instead, the effect of background fluctuations on faint source estimates can be quite pronounced.

In Fig. 12, we provide an example of the estimated source positions and extensions on the simulated data with small background, utilizing the exponential prior pdf. The errors on the estimated parameters are not considered in this plot. Some of the detected faint sources look uncentred and distorted. Four false positives in source detection are found. The simulated data without Poisson noise with the simulated source shapes superimposed are shown for comparison.

Table 3 reports the number of detected sources for each simulation. Different columns are used for accounting true detections and false positives separately. The number of detected sources employing the inverse-Gamma function prior is larger with respect to the exponential prior case only when the cut-off parameter is set lower than the mean background amplitude.

In Fig. 13, the estimated source counts are related to their resolution of source detection (panels a and c) and their source probability (panels b and d) for the simulated data with small background. These are log-linear plots. The results utilizing the exponential and the inverse-Gamma function prior pdfs are shown in panels (a) and (b) and in panels (c) and (d), respectively. The asterisks indicate true sources, while the squares show spurious detections.

The effect of the cut-off parameter $a$ on source detection is visible in panel (c). In this example, the value of $a$ is chosen larger than the simulated background amplitude. Hence, the inverse-Gamma function prior pdf does not allow to detect sources as faint as the exponential prior.

The plots on panels (a) and (c) denote the source detection technique at several correlation lengths. In both plots, a line is drawn
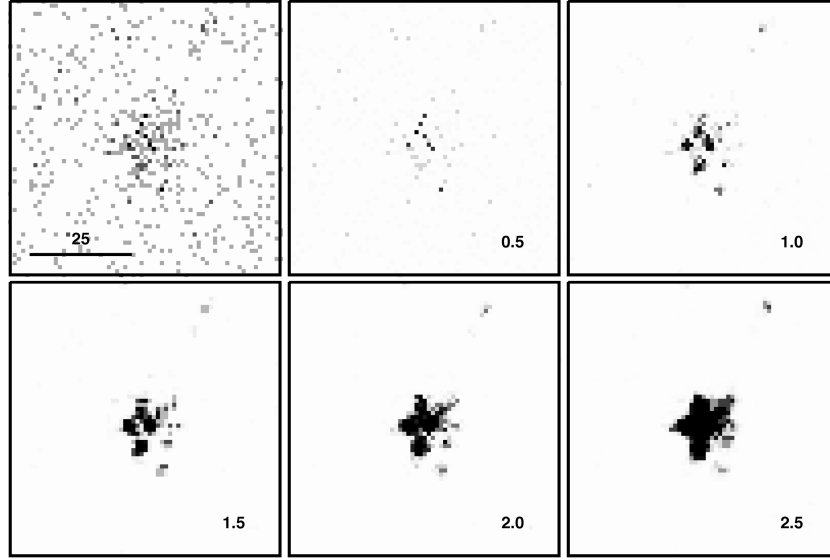
**Figure 11.** The upper left-hand image is a zoom in of the photon count image (panel a, Fig. 8) on a simulated source located at $(x, y) = (360, 270)$. The width of the photon count image is 65 pixels. The following images are SPMs at decreasing resolutions. The correlation length of each SPM is written on the lower right-hand corner of each image in pixel units.
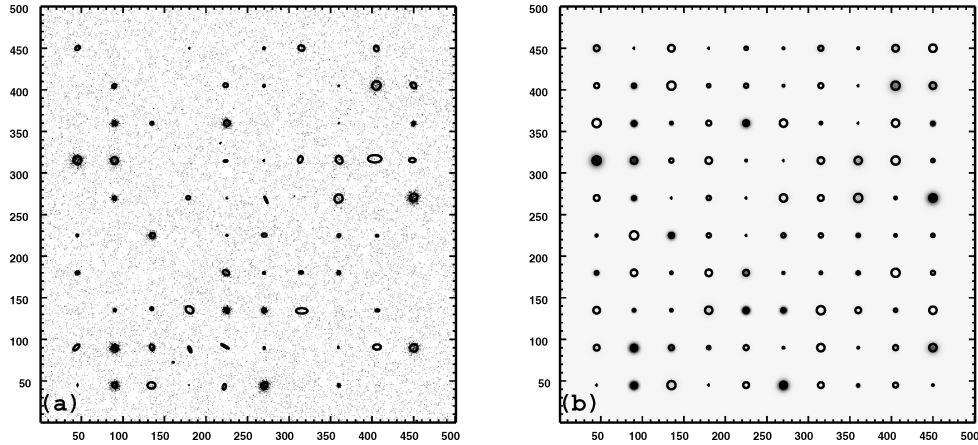


**Figure 12.** Panels (a)–(b): simulated data with small background with and without Poisson noise, respectively, and scaled in the range (0–3) counts. The catalogue obtained employing the *exponential prior* pdf (a) and the shapes of the region of the simulated sources (b) are superposed.

**Table 3.** Source detections on simulated data employing different prior pdfs of the source signal.

| Simulated data | Prior pdf | True detect | False positives | | |
| --- | --- | --- | --- | --- | --- |
| | | | $\geq 50$ per cent | $\geq 90$ per cent | $\geq 99$ per cent |
| 0.1 | Epr | 64 | 4 | 3 | 1 |
| | IGpr | 57 | 7 | 1 | 0 |
| 1.0 | Epr | 41 | 6 | 3 | 0 |
| | IGpr | 42 | 10 | 2 | 0 |
| 10.0 | Epr | 25 | 0 | 0 | 0 |
| | IGpr | 26 | 2 | 2 | 2 |

Note. The background value of the simulated data are reported in counts pixel$^{-1}$. Epr and IGpr have same meaning as given in Fig. 10. The term 'true detect' provides the number of detected sources matched with the simulations. They are catalogued if their probabilities are larger than 50 per cent. The number of 'false positives' in source detection is listed considering 50, 90 and 99 per cent probability thresholds.
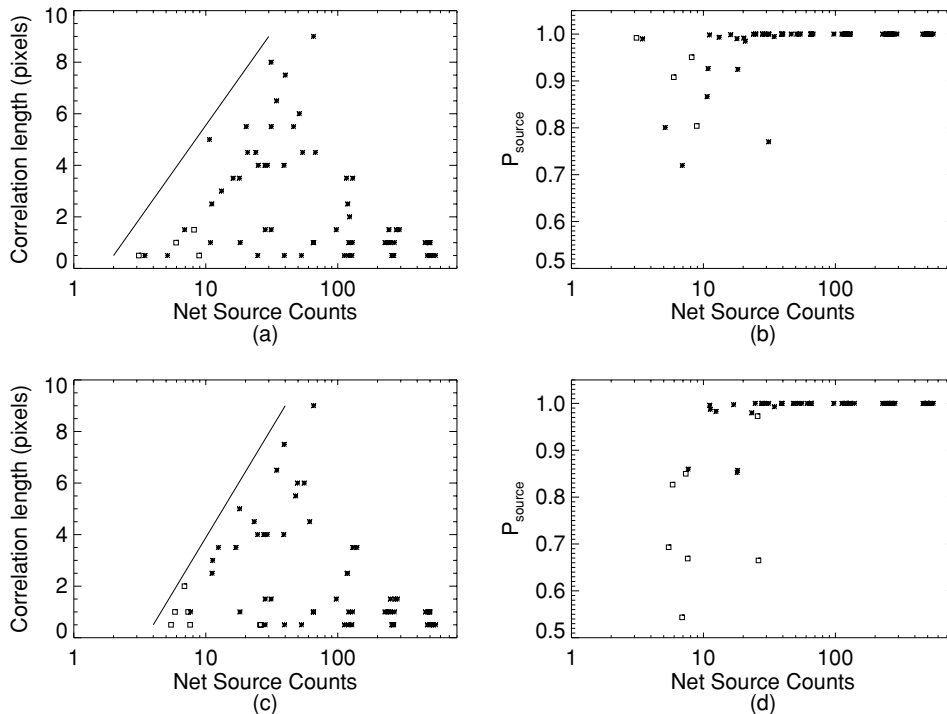
**Figure 13.** Results on simulated data with small background employing the *exponential prior* pdf (panels a and b) and the *inverse-Gamma function prior* pdf (panels c and d). Panels (a) and (c): correlation length in pixel units versus the net source counts. Panels (b) and (d): source probability versus net source counts. Sources matched with the simulated input catalogue are indicated with an asterisk. A square indicates false positives in source detection.

only with the purpose to guide the eye. Left to the line – sources cannot be detected. Right to the line – sources can be found. Very faint sources with few photon counts ($\leq 10$) are resolved by small correlation lengths. In the range (10–100) net source counts, sources are detected at decreasing resolutions. Bright sources do not require large correlation lengths for being detected.

The plots in panels (b) and (d) of Fig. 13 highlight that most of the detections occurs at probabilities larger than 99 per cent. At this probability value and larger, sources matched with the simulated one are strongly separated from false positives.

In Fig. 14 we show the relation between the simulated and the estimated source parameters. Good estimates in source parameters are achieved. The estimated net source counts errors and extension errors can be large for faint sources.

In Fig. 15 a summary on the analysis of all the detected sources employing the exponential prior on the three simulated data sets is presented. The plot in panel (a) shows the difference between estimated and simulated net source counts, normalized with the estimated errors, versus the source probability of the merged data. This plot does not contain the information provided by false positives in source detection. 87 per cent of all detections occurred with probability larger than 99 per cent. The image in panel (b) is a semilog plot of the normalized difference between measured and simulated net source counts versus the simulated net source counts of 98.5 per cent true sources detected in the three simulations. The values of two sources, detected in the simulated data with large background, are outside the selected *y* range. These two detections are included in the analysis of verification with existing algorithms (Section 7). The residuals are normally distributed, as expected. They are located symmetrically around zero. At the faint end, the results are only limited by the small number of simulated faint detectable sources. Faint and bright sources are equally well detected.

### 6.2.6 False positives

Until now we have discussed the detections that have counterparts with the simulated data. We consider now the detection of false positives.

In Table 3 the number of detected false positives are listed for each simulation. At 50 per cent probability threshold more false positives are found with the inverse-Gamma function prior compared to the exponential one. At a 90 per cent source probability threshold, the analyses with the two prior pdfs provide similar results. True detections are strongly separated from statistical fluctuations for source probability values larger than 99 per cent.

When employing the inverse-Gamma function prior pdf, the number of false positives is sensitive to the cut-off parameter. Less false positives are found when *a* is set larger than the background, because it reduces the number of detectable faint sources. It may be worth noting that even when the cut-off parameter is set larger than the background, a probability threshold $\geq 90$ per cent has to be considered (see Fig. 13 for more details).

False positives in source detections show large errors in their estimated parameters. The source probability variation and the source features analyses in the multiresolution technique provide hints of ambiguous detections. However, as all methods, the BSS approach is limited by statistics. Spurious detections cannot be ruled out.

### 6.2.7 Choice of the prior pdf of the source signal

The big difference between the two prior pdfs of the source signal follows on from one prior pdf having one parameter and the other pdf having two.

The parameter $\lambda$, indicating the mean intensity in an astronomical image, introduced with the exponential prior pdf is estimated from the data.
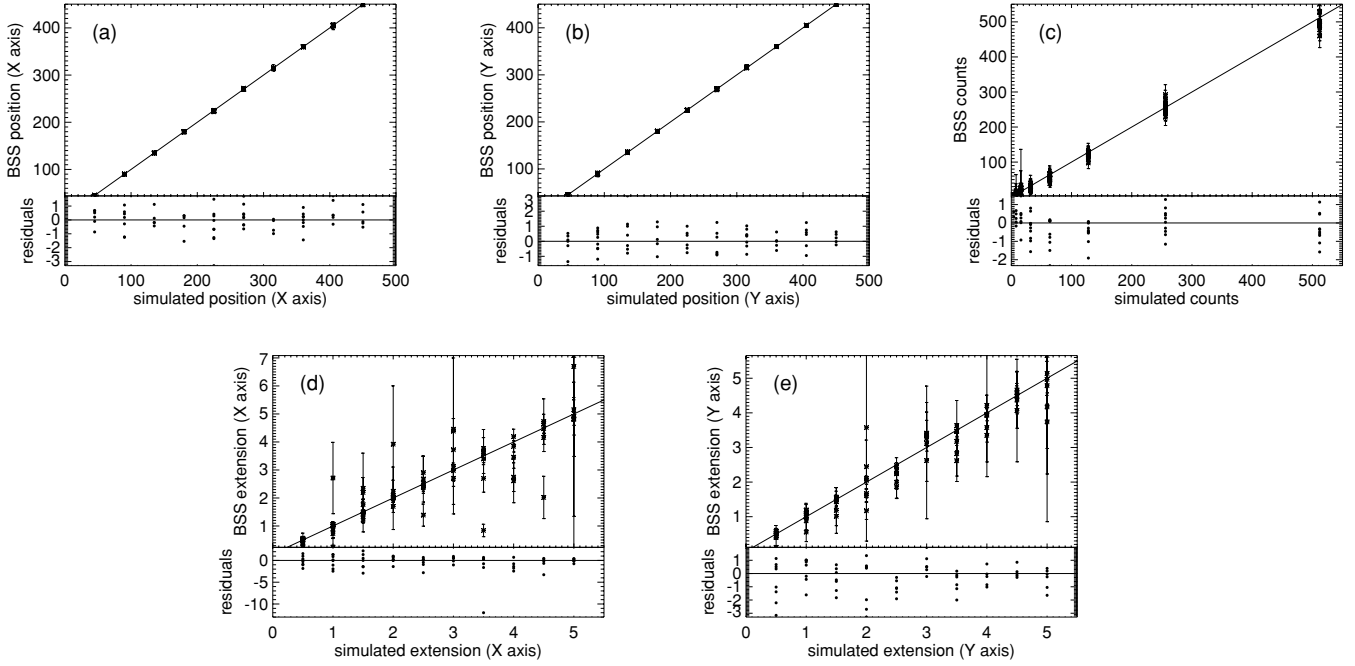
**Figure 14.** Relation between the simulated sources with small background and the measured sources as in output from the processing with the developed method employing the *exponential prior* pdf. Panels (a) and (b) show the comparison of the measured source positions with the simulated input positions on the *x*-axis and on the *y*-axis. Panel (c) displays the relation of the measured source photon counts versus the simulated intensities. A comparison of the estimated source extensions $\sigma_x$ and $\sigma_y$ with the input source extensions are displayed in the panels (d) and (e). The errors estimated for the source parameters are overplotted. The error bars on the estimated values denote the 68 per cent confidence limit of the corresponding posterior distribution. The lower panel in each image shows the fractional residuals.
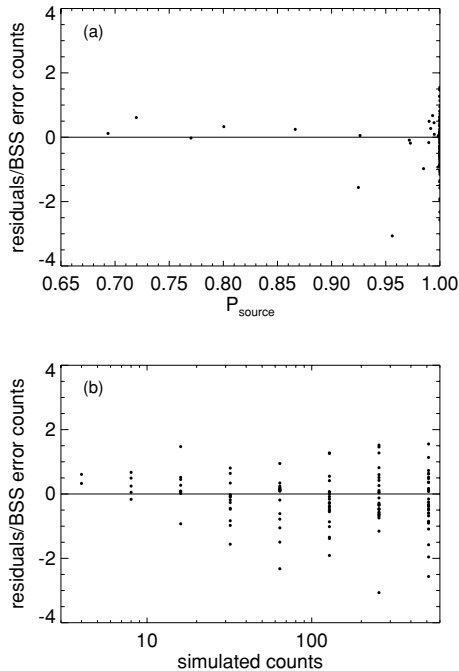


**Figure 15.** Merged information from three simulated data sets of the detected sources employing the *exponential prior* pdf. Panel (a): difference between estimated and simulated net source counts normalized by the errors on the estimated net source counts versus source probability. Panel (b): difference between estimated and simulated net source counts normalized by the errors on the estimated net source counts versus the simulated counts.

The parameter $\alpha$, that is the shape parameter of the power law, given by the inverse-Gamma function prior pdf is estimated from the data. Instead the cut-off parameter *a* is selected to a small value such that the inverse-Gamma function prior pdf behaves as a power law. Astronomical images can be characterized by a small background. It results that *a* can be chosen from a number of alternatives, ranging from values that are above or below the background amplitude. The choice of *a* implies a selection on the detectable sources: sources whose intensity is lower than *a* are not detected; sources close to the background amplitude are detected when *a* is set below the background amplitude.

On real data much more prior information for the cut-off parameter is needed. The inverse-Gamma function prior pdf can be employed if a mean value of the background amplitude is already known from previous analyses.

The exponential prior pdf is preferable over the inverse-Gamma function prior pdf, since no predefined values are incorporated. This is also supported by the results obtained with the simulated data. However, the inverse-Gamma function prior is a more suited model to fit the data and it has potentials for improving the detections of faint objects.

One way to improve the knowledge acquired with the inverse-Gamma function prior is by the estimation of the cut-off parameter from the data. This change in our algorithm is not straightforward and MCMC algorithms have to be employed.

### 6.3 Summary

Simulated data are employed to assess the properties of the BSS technique. The estimated background and source probabilities depend on the prior information chosen. A successful separation of background and sources must depend on the criteria which define

*background*. Structures beyond the defined properties of the background model are, therefore, assigned to be sources. There is no sensible background-source separation without defining a model for the object *background*. Additionally, prior information on source intensity distributions helps to sort data, which are marginally consistent with the background model, into background or source. Therefore, prior knowledge on the background model as well as on the source intensity distribution function is crucial for successful background–source separation.

For the background model a two-dimensional TPS representation was chosen. It is flexible enough to reconstruct any spatial structure in the background rate distribution. The parameters are the number, position and amplitudes of the spline supporting points. Any other background model capable to quantify structures which should be assigned to background can be used as well.

For the prior distribution of the source intensities the exponential and the inverse-Gamma function are used as illustrations. For both distributions the source probability can be given analytically. The hyperparameters of both distributions can either be chosen in advance to describe known source intensity properties or can be estimated from the data. If they are estimated from the data simultaneously with the background parameters, properties of the source intensity distribution can be derived, but at the expense of larger estimation uncertainties. It is important to note that the performance of the BSS method increases with the quality of prior information employed for the source intensity distribution. The prior distribution of the source intensities determines the general behaviour of the sources in the field of view and the hyperparameters are useful for fine-tuning.

The aim of detecting faint sources competes with the omnipresent detection of false positives. The suppression of false positives depends both on the expedient choice of prior information and on the level of detection probability accepted for source identification. Compared to e.g. *p* values the BSS technique is rather conservative in estimating source probabilities. Therefore, a probability threshold of 99 per cent is mostly effective to suppress false positives.

The estimated background rates are consistent with the simulated ones. Crowded areas with regions of marginally detectable sources might increase the background rate accordingly.

The SPMs at different correlation lengths are an important feature of the technique. The multiresolution analysis allows one to detect fine structures of the sources.

The source parameters are well determined. Their residuals are normally distributed. We will show in Section 7 that the BSS technique performs better than frequently used techniques. Naturally, the estimation uncertainties of parameters for faint sources are large due to the propagation of the background uncertainty.

# 7 VERIFICATION WITH EXISTING ALGORITHMS

In the X-ray regime, the sliding window technique and the WT techniques are widely used. However, the WT has been shown to perform better than the sliding window technique for source detection. The WT improvement in source detection with respect to the sliding window technique is inversely proportional to the background amplitude (Freeman et al. 2002). The WT has also other favourable aspects for being compared with the BSS method developed in our work. The WT allows for the search of faint extended sources. The BSS method with the multiresolution technique is close to the WT method.

**Table 4.** Number of detected sources employing WAVDETECT on three simulated data sets.

| Simulated data | True detect | False positives |
|---|---|---|
| 0.1 | 56 | 4 |
| 1.0 | 37 | 1 |
| 10.0 | 23 | 1 |

Note. The explanation of these columns can be found in Table 3.

Between all the available software employing WT, we choose WAVDETECT (Freeman et al. 2002), part of the freely available CIAO software package. We use version 3.4.

WAVDETECT is a powerful and flexible software package. It has been developed for a generic detector. It is applicable to data with small background. The algorithm includes satellite's exposure variations. It estimates the local background count amplitude in each image pixel and it provides a background map.

We utilize WAVDETECT on our simulated data described in Section 6. The threshold setting for the significance ('sigthresh') is chosen equal to $4.0 \times 10^{-6}$, in order to detect on the average 1 spurious source per image. The 'scale' sizes are chosen with a logarithmic increment from 2 to 64. Tests have been made changing the levels of these parameters, assuring us that the selected values provide good performance of this WT technique. In Table 4, we report the number of detected sources per simulated field, separating the sources matched with the simulated one (*true detect*) to the false positives in source detection found employing the above mentioned threshold setting. The three simulated data sets are distinguished by their background values (counts). The simulated background values are reported in column *simulated data*. These results are compared with the ones obtained with the BSS algorithm when employing the exponential prior pdf as shown in Table 3.

The BSS technique finds all sources detected by WAVDETECT. In the simulated data characterized by small background, the two algorithms find the same number of false positives. The BSS algorithm reveals 8 per cent more true detections than WAVDETECT. These sources are characterized by counts in the range (4–8). Hence, the BSS technique performs better than WAVDETECT in the low number counts regime. The performance of the two techniques on the data sets with intermediate and large background values is similar.

The explanation for these results is enclosed in the background estimate. The WAVDETECT estimates of background values are similar to the results obtained with the BSS technique in the intermediate and large background data sets. Though, the backgrounds provided by WAVDETECT present rings due to the Mexican Hat function employed as a filter on the image data. In the simulated data with small background, the WAVDETECT background model is on the average larger than the one estimated with the BSS method. The plots in Fig. 16 support these conclusions (semilog plots). The image in panel (a) shows that WAVDETECT fluxes are underestimated for ∼20 per cent of all detected sources. In addition, WAVDETECT sensitivity for source detection is limited to 16 counts per source within these simulated data sets. Fig. 15, panel (b), presents the sensitivity achieved by the BSS method. The plot in panel (b) of Fig. 16 displays a relation between the sources detected by WAVDETECT (ordinate) and by BSS (abscissa), both matched with the simulated data. Most of the WAVDETECT underestimated sources are coming from the simulated data with small background. BSS presents only two sources underestimated and detected in the simulated data with
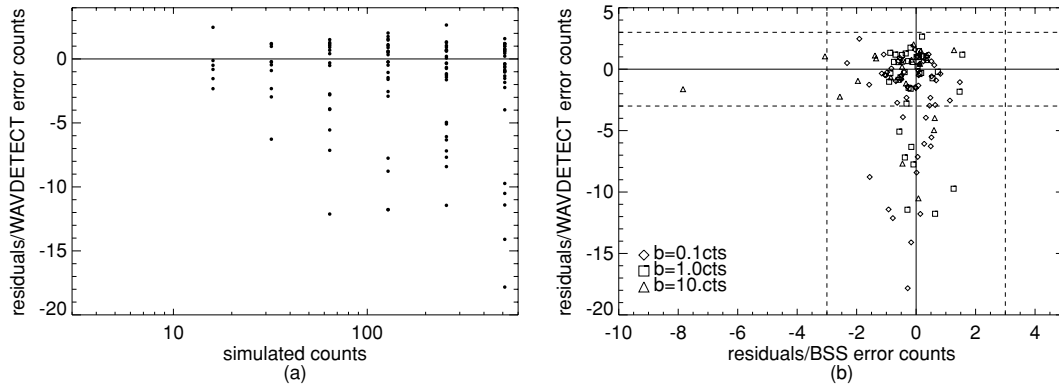
**Figure 16.** Panel (a): normalized difference between WAVDETECT estimated source counts versus simulated counts of all the detected sources in the three simulated data sets. Panel (b): comparison between the normalized differences of WAVDETECT source counts and simulated counts, on the ordinate, and the normalized difference of BSS source counts and simulated counts, on the abscissa. Sources detected from the simulated data with small background are indicated with a diamond. A square is used to highlight sources detected in the data set with intermediate background. The detected sources in the simulated data with large background are indicated with a triangle. Dashed lines are drawn as a borderline of the $\pm 3\sigma$ detection. The zero line is indicated with a continuous line style.
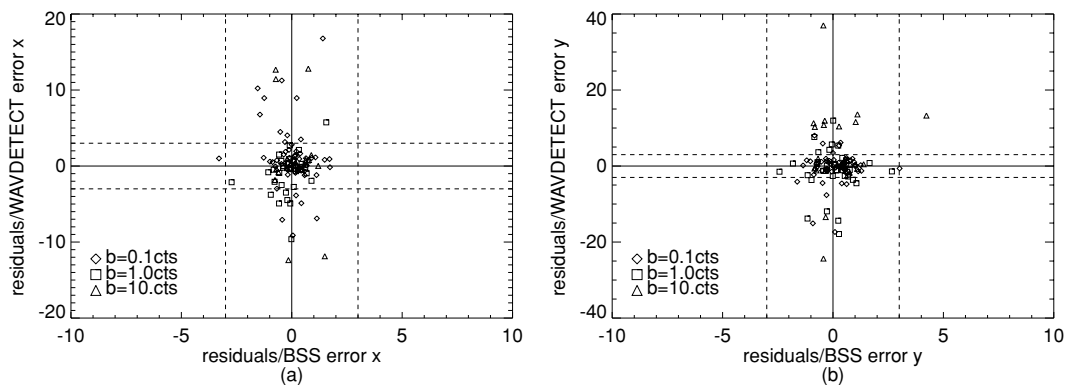


**Figure 17.** Same explanation as for panel (b) in Fig. 16, but comparing the estimated source positions: *x*-axis (panel a); *y*-axis (panel b).

large background. By chance, the triangle located at $(-8, -2)$ indicates the detection of two sources. Both sources where simulated with 256 source counts and a circular extension of 4 pixels one, 5 pixels the other. The estimated source positions are also improved with BSS (Fig. 17, semilog plots).

The residuals provided by the BSS technique are a factor of 10 smaller than the ones from WAVDETECT. Their estimates have many outliers. Our estimates are normally distributed.

Though the comparison between the two detection methods is not yet carried out on real data, these results are encouraging. The BSS method detects at least as many sources as WAVDETECT. The simulations prove that the developed Bayesian technique ameliorates the detections in the low count regime. The BSS estimated positions and counts are improved. Finally, we expect that the BSS technique will refine WAVDETECT sensitivity on real data, because the BSS technique is designed for modelling highly and slowly varying backgrounds taking into account instrumental structures.

## 8 APPLICATION TO OBSERVATIONAL DATA

In this section we employ RASS data to show the effectiveness of our method at large varying background, exposure values and where exposure non-uniformities are consistently taken into account. We present results obtained combining SPMs at different energy bands.

We demonstrate that our algorithm can detect sources independently of their shape, sources at the field's edge and sources overlapping a diffuse emission. Last, the BSS technique provides evidence for celestial sources not previously catalogued by any detection technique in the X-ray regime.

### 8.1 *ROSAT* PSPC in survey mode data

We apply the BSS algorithm on a data sample coming from the Position Sensitive Proportional Counter (PSPC) on board of the *ROSAT* satellite in survey mode (0.1–2.4 keV). *ROSAT* satellite provided the only all-sky survey realized using an imaging X-ray telescope (Voges et al. 1999, 2000).

RASS data supply a unique map of the sky in the X-ray regime. The map of the sky was divided in 1378 fields each of $6.4° \times 6.4°$, corresponding to $512 \times 512$ pixels. In addition, the satellite's exposure time can vary between about 0.4 and 40 ks and some parts of the sky are without observations due to the satellite's crossing of the auroral zones and of the South Atlantic Anomaly. Therefore, RASS data provide a wide range of possibilities for testing the BSS algorithm.

We present the results obtained analysing three *ROSAT* fields, whose IDs are RS930625n00, RS932209n00 and RS932518n00.
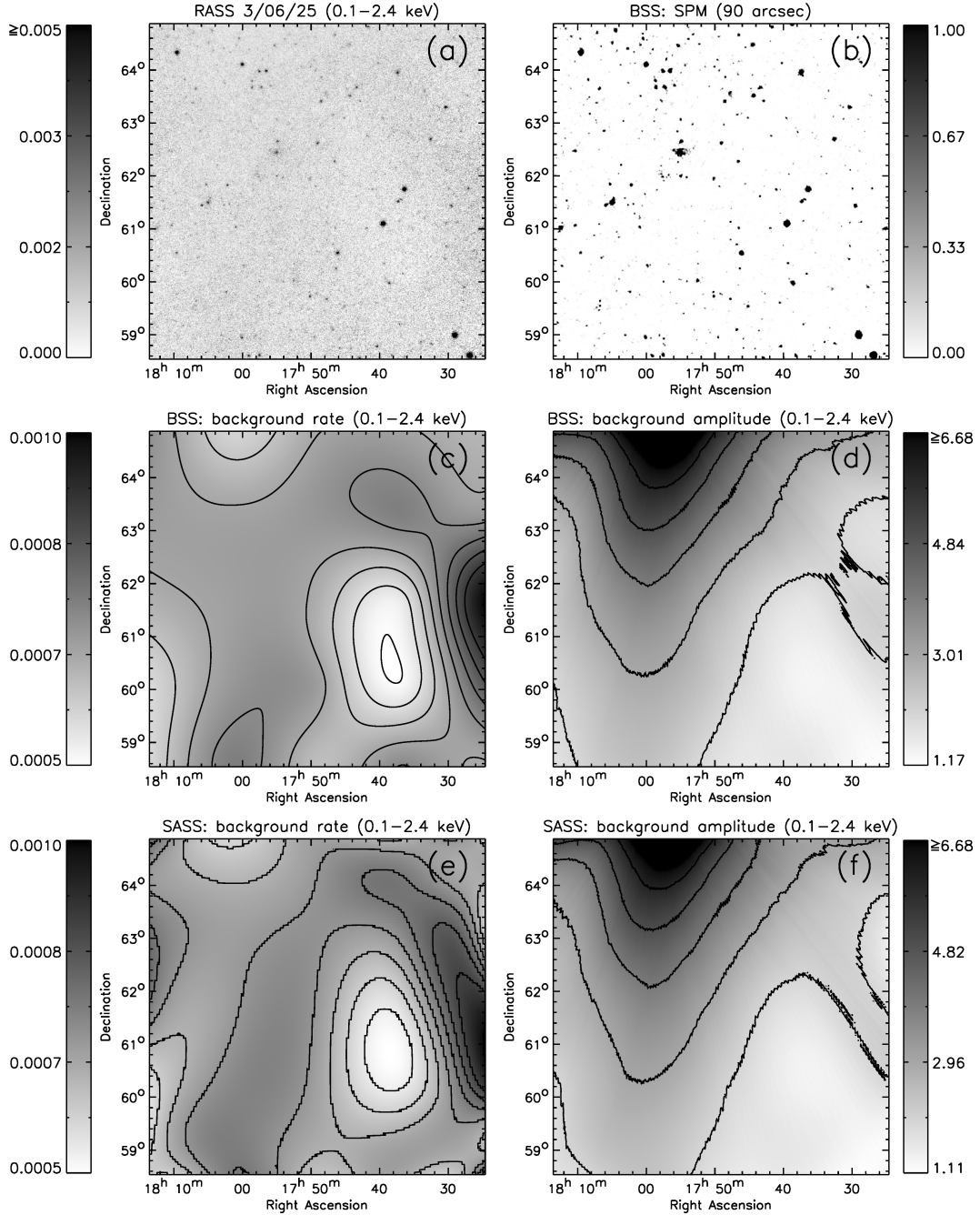
**Figure 18.** Analysis of RS930625n00, *ROSAT* PSPC in survey mode field.

### 8.1.1 RS930625n00

This *ROSAT* field is located at $\alpha = 17^h49^m5^s$, $\delta = +61°52'30''$. It is characterized by large variations of the satellite's exposure ranging from 1.7 to 13.5 ks. The count rate image of RS930625n00 in the broad energy band (0.1–2.4 keV) is displayed in panel (a) of Fig. 18. The count rates range over (0.–0.11) photon count s$^{-1}$ pixel$^{-1}$. The image is here scaled in the range (0.–0.005) photon count s$^{-1}$ pixel$^{-1}$ in order to enhance the sources.

Our results employing the BSS algorithm are shown in Fig. 18 with a SPM, the TPS map and the background map.

In panel (b), the SPM is obtained combining statistically the soft (0.1–0.4 keV) and the hard (0.5–2.4 keV) energy bands. The

SPM here displayed is obtained employing the exponential prior pdf and accounts for the width of the *ROSAT* instrumental PSF. The information of pixels is combined with the box filter method with the cell shape of a circle. This image corresponds to a correlation length of 1.5 arcmin. Sources are identified in terms of probabilities. The image is in linear scale.

In panel (c), the TPS map is modelled from RS930625n00 field, broad energy band. The TPS models the background rate. Only 25 support points are used. The background rate ranges (0.0005–0.001) photon count s$^{-1}$ pixel$^{-1}$. The contours are superposed for enhancing the features relative to the modelled background rate. The innermost and the outermost contours indicate a level of 0.0005 and 0.001 photon count s$^{-1}$ pixel$^{-1}$, respectively.
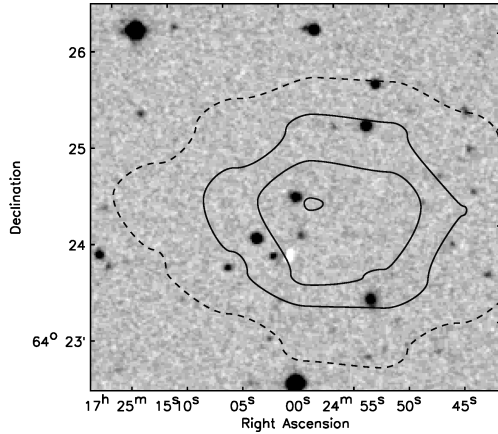
**Figure 19.** POSS-II red plate with overlaid *ROSAT* contours corresponding to 3, 4, 4.5 and 5σ above the local background. In the image centre is located SDSS J172459.31+642424.0, a low-redshift QSO.

The corresponding background map estimated from the selected *ROSAT* field is displayed in panel (d). Its values are in the range (1.17–8.53) photon count pixel$^{-1}$. The image is scaled in the range (1.17–6.68) photon count pixel$^{-1}$. The contour levels close to black and light grey delineate 6.0 and 2.0 photon count pixel$^{-1}$, respectively. The background map shows the prominent variation due to the heterogeneous satellite exposure time.

The lower row of Fig. 18 shows the background rate (panel e) and the background amplitude (panel f) as obtained analysing the broad energy band with the Standard Analysis Software System (SASS). SASS is the detection method utilized for the realization of RASS. SASS combines the sliding window technique with the maximum likelihood PSF fitting method for source detection and characterization, respectively. The background rate image is in the range (0.0005–0.00097) photon count s$^{-1}$ pixel$^{-1}$. The innermost and the outermost contour levels delineate 0.0006 and 0.0009 photon count s$^{-1}$ pixel$^{-1}$, respectively. The background amplitude image estimated by SASS has values in the range (1.11–8.27) photon count pixel$^{-1}$. The image is scaled as the one obtained from the BSS technique. The contour levels indicate from 2.0 to 6.0 photon count pixel$^{-1}$.

The BSS technique allows for more flexibility in the background model and the edges are more stable than the ones obtained with

SASS. Hence, celestial objects located on the edges are not lost during source detection.

In Fig. 19 we show an example of a QSO detection with the BSS algorithm analysing the field RS930625n00 in the hard (0.5–2.4 keV) band image. No counterparts have been found in the *ROSAT* bright and faint source catalogues (Voges et al. 1999, 2000). A counterpart is found with the Sloan Digital Sky Survey (SDSS). This QSO is catalogued as SDSS J172459.31+642424.0 (Abazajian et al. 2004; Hao et al. 2005, Vanden Berk et al. 2006). It is located at the image centre. The image covers a field of view of ∼5 arcmin at the side. The *ROSAT* image, as shown in Fig. 18, has 45 arcsec pixel$^{-1}$ resolution. The QSO optical position as given by the SDSS is 12 arcsec far from the BSS position, i.e. it is within the pixel resolution of the *ROSAT* data. The estimated source count rate with the BSS algorithm for this source is (0.0068 ± 0.0023) photon count s$^{-1}$. Its source detection probability is 0.999. This object is located close to the north-west corner of the field RS930625n00 (∼45 arcmin). In this region the SASS background intensity is 7 per cent lower than the BSS background estimate.

### 8.1.2 RS932209n00

The detection capabilities of our Bayesian approach on images with exposure non-uniformities are presented in Figs 20 and 21. The analysed *ROSAT* field is located at $\alpha = 3^h 31^m$, $\delta = -28°07'08''$.

In Fig. 20, panel (a), the soft band image (0.1–0.4 keV) is shown. The image accounts for photon count pixel$^{-1}$ in the range (0–9). The image is scaled in the range (0–2) photon count pixel$^{-1}$. In panel (b), an SPM as in output from the BSS method is displayed. The inverse-Gamma function prior pdf is used for source detection and background estimation. This SPM is obtained with a correlation length of 270 arcsec. The box filter method with the cell shape of a circle is employed. The SPM shows source detections.

In Fig. 21, panel (a), the satellite's exposure is located. The exposure values are in the range (0–0.393) ks. In panel (b) we show the background map estimated with the developed BSS technique. Only 16 pivots equidistantly distributed along the field are employed. The background amplitude ranges from 0 to 0.318 photon count pixel$^{-1}$. The background is estimated with null value where no satellite's exposure information is provided. The estimated background map is similar to the exposure map because the contribution from the cosmic background is very small.
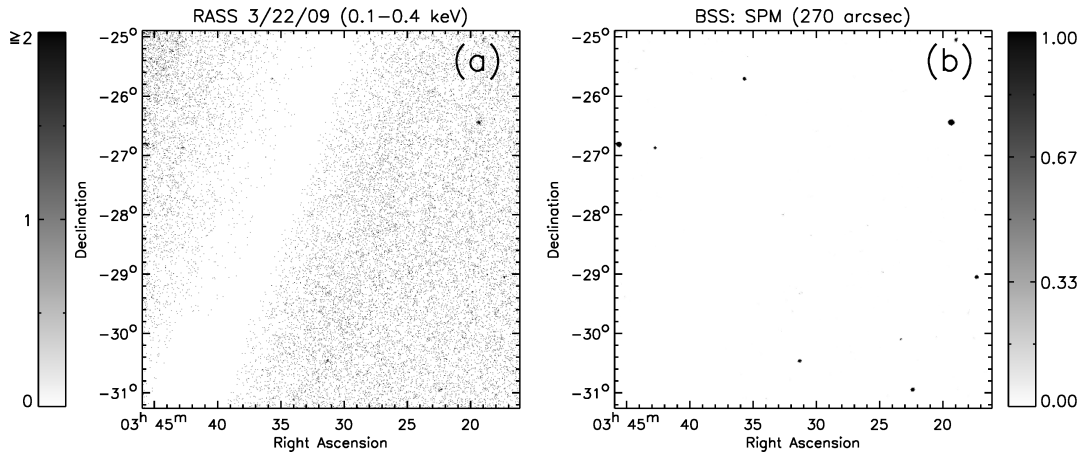


**Figure 20.** Panel (a): *ROSAT* All-Sky Survey *photon count image* of the field id RS932209n00 in the soft energy band. Panel (b): *source probability map* as obtained with the developed BSS method.
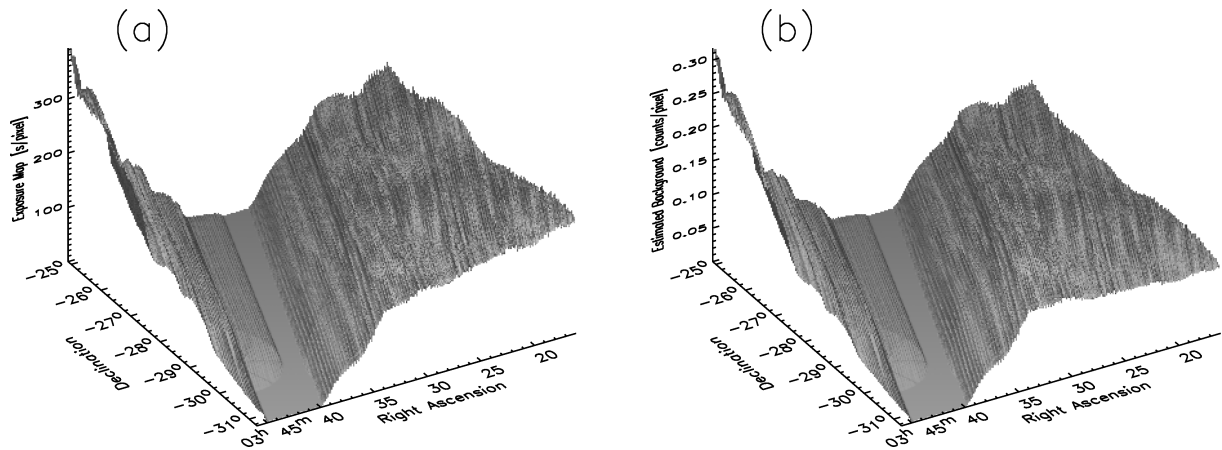
**Figure 21.** Panel (a): *exposure map* of the *ROSAT* field id RS932209n00 (Fig. 20). The *z*-axis indicates the exposure time in s pixel$^{-1}$. Panel (b): *estimated background amplitude* with the BSS technique of RS932209n00 field in the soft energy band. The *z*-axis shows the estimated background count pixel$^{-1}$.

No artefacts, due to exposure non-uniformities, occur in the background map nor in the SPMs.

### 8.1.3 RS932518n00

We employ the *ROSAT* field id RS932518n00 in the hard energy band (0.5–2.4 keV) to show the capabilities of our technique on data with large background variations. This field is characterized by a complex structure of hot gas caused primarily by the emissions of two galactic X-ray sources: (1) Vela supernova remnant (SNR) located at $\alpha = 8^{\mathrm{h}}35^{\mathrm{m}}20\overset{\mathrm{s}}{.}6, \delta = -45°10'35''$; (2) SNR RX J0852.0−4622 located at $\alpha = 8^{\mathrm{h}} 52^{\mathrm{m}}, \delta = -46°22'$, see Aschenbach, Egger & Trümper (1995) and Aschenbach (1998).

In Fig. 22, panel (a), we display the photon count image of RS932518n00 field in the hard energy band. The image presents values in the range (0–136) photon count pixel$^{-1}$. It is scaled in the range (0–15) photon count pixel$^{-1}$ in order to enhance the X-ray emissions. The satellite's exposure map is displayed in Fig. 23, panel (a). The exposure map shows variations in the range (0.5–0.8) ks.

The analysis of RS932518n00 in the hard energy band with the BSS algorithm is shown in Figs 22, panels (b)–(d), and 23, panel (b). For background estimation and source detection the exponential prior pdf is employed.

In Fig. 22, panels (b)–(d), three SPMs are displayed. The correlation lengths used for their realization is written on each image. The information of neighbouring pixels is put together with the Gaussian weighting method. These SPMs are in linear scale.

The background map (Fig. 22, panel b) is estimated utilizing 36 pivots equidistantly spaced along the field. The estimated background values range from ∼0 to 4.1 photon count pixel$^{-1}$. The heterogeneous background is recovered.

The BSS method combined with the multiresolution analysis allows one to identify the detection of point-like sources on top of the diffuse emission and of extended X-ray features, such as the Pencil Nebula located at $\alpha = 9^{\mathrm{h}}0.2^{\mathrm{m}}, \delta = -45°57'$ and the SNR RX J0852.0−4622. The BSS algorithm detects about 50 objects on this *ROSAT* field.

In Table 5 we present part of this catalogue. Columns RA, Dec., Sctr, $\sigma_x$, $\sigma_y$ and $\rho$ are the estimated positions, source count rates and source parameters as in output from the developed BSS technique. Each listed object is detected with a probability larger then 0.999.

The column indicated with $matched\,ID$ corresponds to an *ID* given by catalogues created analysing *ROSAT* data and whose position matches with the one obtained with the BSS algorithm. During this selection, we give priority to IDs provided by RASS catalogues when available. Catalogues IDs highlighted with a *b* are coming from a point source catalogue generated from all *ROSAT* PSPC pointed observations.

## 9 CONCLUSIONS

We have presented a new statistical method for source detection, background estimation and source characterization in the Poisson regime. With this technique we have elaborated a very general and powerful Bayesian method applicable to images coming from any count detector. It is particularly suitable for the search of faint and extended sources in images coming from instruments of a new generation. We apply our technique to X-ray data.

The developed technique does not loose information from the data and preserves the statistics. The BSS algorithm provides a comprehensive error analysis where uncertainties are properly included in the physical model.

The background and its errors are estimated on the complete field with a two-dimensional spline and the knowledge of the experimental data and the exposure map. The background model is well defined along the complete field, so that field edges and instrumental effects are correctly handled and sources located at the edges or gaps are not penalized.

The BSS method does not assume anything about the source size or shape for an object to be detected. Sources are separated from the background employing BPT combined with the mixture model technique. Point-like and extended sources are detected independent from their morphology and the kind of background. Consequently, the BSS technique can be applied to large data volumes, e.g. surveys from *X*-ray missions.

We developed the BSS technique utilizing two prior pdfs of the source signal. We proved that the prior pdfs of the source signal allow one to select what has to be described as source or as background.

The SPMs are robust features of our technique. They allow for the analysis of faint and extended objects. SPMs obtained at different energy bands can be combined probabilistically providing conclusive likelihoods for each detected source.
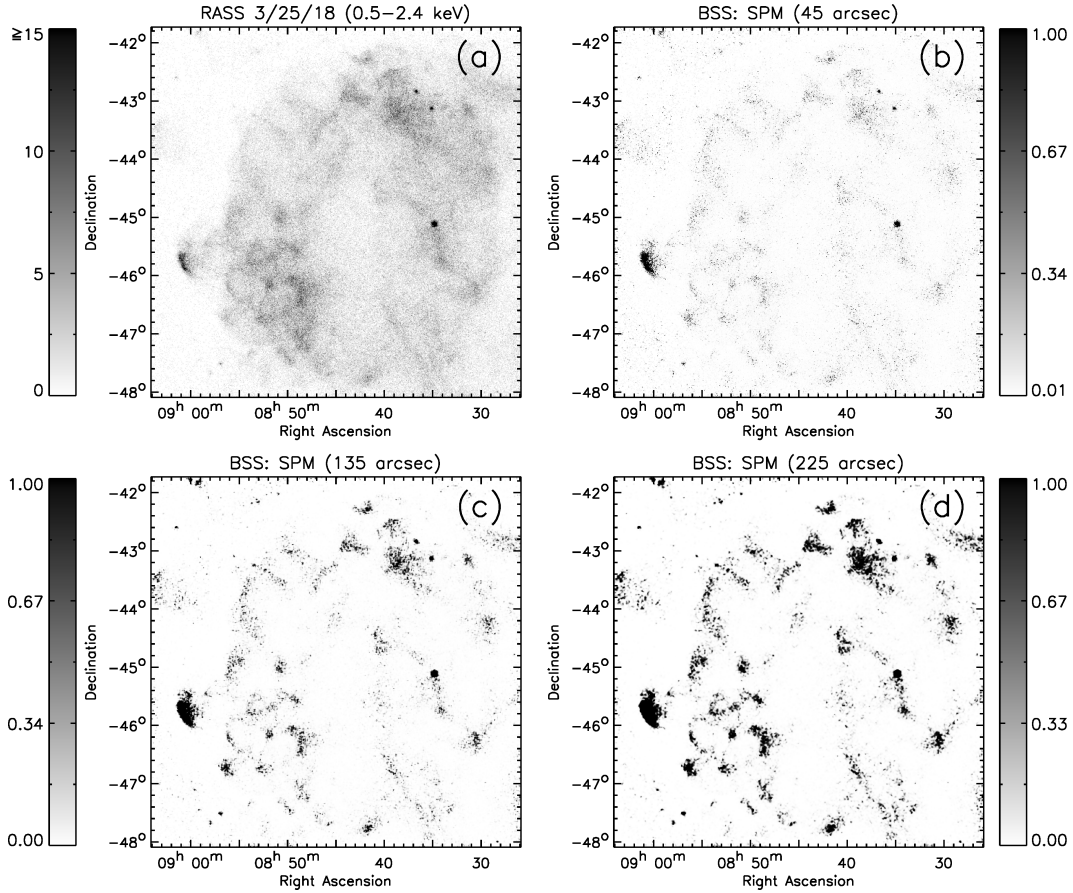
**Figure 22.** Panel (a): *ROSAT* All-Sky Survey *photon count image* of the field id RS932518n00 in the hard energy band. The analysis of this *ROSAT* field with the developed BSS method is shown in panels (b)–(d) with SPMs obtained with increasing correlation lengths.
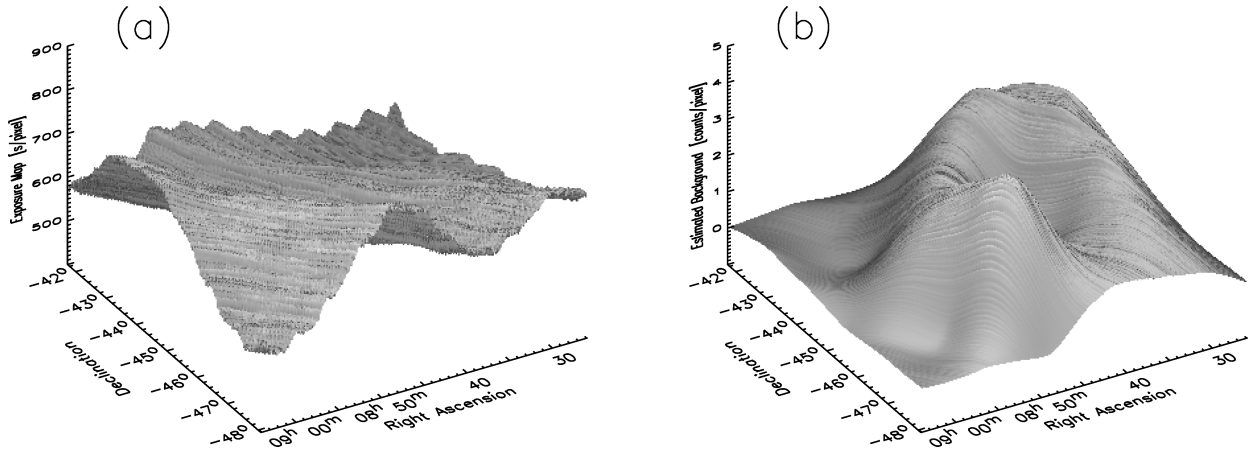


**Figure 23.** Panel (a): *exposure map* of the *ROSAT* field id RS932518n00 (Fig. 22). The *z*-axis indicates the exposure time in $\mathrm{s\,pixel^{-1}}$. Panel (b): *estimated background amplitude* with the BSS technique of RS932518n00 field in the hard energy band. The *z*-axis shows the estimated background count $\mathrm{pixel^{-1}}$.

The BSS photometry is robust. The errors on the estimated source parameters are normally distributed.

We demonstrated that our technique is capable of coping with spatial exposure non-uniformities, large background variations and of detecting sources embedded on a diffuse emission. We expect to handle consistently the heterogeneities present in astronomical images with CCD patterns, images superposed and mosaic of images.

Finally, the verification procedure with existing algorithms through simulations demonstrates that the BSS technique improves the detection of sources with extended low surface brightness. This is supported by the applications on real data. The BSS method has good potentials for improving, first, the count rate of detected sources and, second, the sensitivity reached by other techniques also on real data.

**Table 5.** BSS sample catalogue from the analysis of RS932518n00 field in the hard energy band (0.5–2.4 keV).

| | RA | Dec. | Sctr (count s$^{-1}$) | $\sigma_x$ (pixel) | $\sigma_y$ (pixel) | $\rho$ | Matched ID |
|---|---|---|---|---|---|---|---|
| (1) | 08$^h$35$^m$20$^s$4 | $-45°10'36''37$ | $2.7259 \pm 0.0745$ | $1.91 \pm 0.05$ | $1.93 \pm 0.05$ | $-0.05 \pm 0.04$ | 1RXS J083520.6$-$451035[a] |
| (2) | 08$^h$37$^m$24$^s$62 | $-42°53'55''75$ | $0.6236 \pm 0.0486$ | $1.49 \pm 0.17$ | $1.56 \pm 0.12$ | $-0.32 \pm 0.10$ | 1WGA J0837.3$-$4253[b] |
| (3) | 08$^h$35$^m$55$^s$85 | $-43°11'11''29$ | $0.7099 \pm 0.0524$ | $1.55 \pm 0.12$ | $1.73 \pm 0.15$ | $0.06 \pm 0.11$ | 1WGA J0835.9$-$4311[b] |
| (4) | 08$^h$57$^m$44$^s$81 | $-41°51'51''52$ | $0.2478 \pm 0.0253$ | $3.20 \pm 0.33$ | $3.60 \pm 0.38$ | $0.07 \pm 0.14$ | 1RXS J085748.6$-$415101[a] |

[a]Voges et al. (1999).
[b]White, Giommi & Angelini (1994).

## 10 ACRONYMS

The following is a list of acronyms frequently appearing in the text.

| | |
|---|---|
| BPT | Bayesian probability theory |
| BSS | background–source separation |
| CCD | charge-coupled device |
| cdf | cumulative distribution function |
| FWHM | full width at half-maximum |
| MCMC | Markov-chain Monte Carlo |
| MPD | Marginal Poisson Distribution |
| PD | Poisson Distribution |
| pdf | probability density function |
| PSF | point spread function |
| PSPC | Position Sensitive Proportional Counter |
| RASS | *ROSAT* All-Sky Survey |
| SASS | Standard Analysis Software System |
| SDSS | Sloan Digital Sky Survey |
| SPM | source probability map |
| SNR | supernova remnant |
| TPS | thin-plate spline |
| WT | wavelet transform |

## REFERENCES

Abazajian K. et al., 2004, AJ, 128, 502
Aschenbach B., 1998, Nat, 396, 141
Aschenbach B., Egger R., Trümper J., 1995, Nat, 373, 587
Becker A. C., Silvestri N. M., Owen R. E., Ivezić Ž., Lupton R. H., 2007, PASP, 119, 1462
Berger J. O., 1997, in Babu G. H., Feigelson E. D., eds, Statistical Challenges in Modern Astronomy II. Springer-Verlag, New York, p. 15
Berger J. O., Berry D., 1988, Am. Sci., 76, 159
Berger J., Delampady M., 1987, Stat. Sci., 2, 317
Berger J., Sellke T., 1987, J. Am. Stat. Assoc., 82, 112
Bernardo J. M., Smith A. F., 1994, Bayesian Theory. Wiley, New York
Bertin E., Arnouts S., 1996, A&AS, 117, 393
Boese F. G., Doebereiner S., 2001, A&AS, 370, 649
Brandt W. N., Hasinger G., 2005, ARA&A, 43, 827
Carvalho P., Rocha G., Hobson M. P., 2009, MNRAS, 393, 681
Cash W., 1979, ApJ, 228, 939
Cavaliere A., Fusco-Femiano R., 1978, A&A, 70, 677
Cruddace R. G., Hasinger G. R., Schmitt J. H., 1988, in Murtagh F., Heck A., eds, Astronomy from Large Databases. ESO, Garching, p. 177
Damiani F., Maggio A., Micela G., Sciortino S., 1997, ApJ, 483, 350
Delampady M., Berger J. O., 1990, Ann. Stat., 18, 1295
Dose V., 2003, Rep. Prog. Phys., 66, 1421
Everitt B. S., Hand D. J., 1981, Finite Mixture Distributions. Chapman & Hall, London
Fischer R., Dose V., 2002, in Fry R.-L., ed., AIP Conf. Proc. Vol. 617, Bayesian Inference and Maximum Entropy Methods in Science and Engineering. Am. Inst. Phys., New York, p. 143
Fischer R., Hanson K. M., Dose V., von der Linden W., 2000, Phys. Rev. E, 61, 1152
Fischer R., Hanson K. M., Dose V., von der Linden W., 2001, in Rychert J. T., Erickson G. J., Smith C. R., eds, AIP Conf. Proc. Vol. 567, Bayesian Inference and Maximum Entropy Methods in Science and Engineering. Am. Inst. Phys., New York, p. 193
Fischer R., Dinklage A., Pasch E., 2003, Plasma Phys. Control. Fusion, 45, 1095
Freeman P. E., Kashyap V., Rosner R., Lamb D. Q., 2002, ApJS, 138, 185
Gelman A., Carlin J. B., Stern H. S., Rubin D. B., 1995, Bayesian Data Analysis. Chapman & Hall, London
Gioia I. M., Maccacaro T., Schild R. E., Wolter A., Stocke J. T., Morris S. L., Henry J. P., 1990, ApJS, 72, 567
Gregory P. C., 2005, Bayesian Logical Data Analysis for the Physical Science: A Comparative Approach with 'Mathematica' Support. Cambridge Univ. Press, Cambridge
Gregory P. C., Loredo T. J., 1992, ApJ, 398, 146
Hao L. et al., 2005, AJ, 129, 1783
Harnden F. R., Jr, Fabricant D. G., Harris D. E., Schwarz J., 1984, SAO Spec. Rep., 393
Hasinger G., Johnston H. M., Verbunt F., 1994, A&A, 288, 466
Hobson M. P., McLachlan C., 2003, MNRAS, 338, 765
Jaynes E. T., 2003, Probability Theory: the Logic of Science. Cambridge Univ. Press, Cambridge
Jeffreys H., 1961, Theory of Probability, 3rd edn. Oxford Univ. Press, Oxford
Kass R. E., Raftery A. E., 1995, J. Am. Stat. Assoc., 90, 773
King I., 1962, AJ, 67, 471
Kolaczyk E. D., Dixon D. D., 2000, ApJ, 534, 490
Linnemann J., 2003, in Lyons L., Mount R., Reitmeyer R., eds, Proc. PHYSTAT 2003 Conf. Statistical Problems in Particle

Physics, Astrophysics, and Cosmology. SLAC eConf C030908, http://www.slac.stanford.edu/econf/C030908, p. 35

Loredo T. J., 1990, in Fougere P. F., ed., Maximum Entropy and Bayesian Methods. Kluwer, Dordrecht, p. 81

Loredo T. J., 1992, in Feigelson E. D., Babu G. J., eds, Statistical Challenges in Modern Astronomy. Springer-Verlag, New York, p. 275

Loredo T. J., Wasserman I. M., 1995, ApJS, 96, 261

Meinguet J., 1979, J. Appl. Math. Phys. (ZAMP), 30, 292

Murtagh F., Raftery A., Starck J.-L., 2005, Image Vis. Comput., 23, 587

Neal R. M., 1992, in Smith C. R., Erickson G. J., Neudorfer P. O., eds, Maximum Entropy and Bayesian Methods. Kluwer, Dordrecht, p. 197

O'Hagan A., Forster J., 2004, Kendall's Advanced Theory of Statistics, Vol. 2B: Bayesian Inference, 2nd edn. Hodder Arnold, London

Pierre M. et al., 2004, J. Cosmol. Astropart. Phys., 9, 11

Rosati P., della Ceca R., Burg R., Norman C., Giacconi R., 1995, ApJ, 445, L11

Rosati P., Borgani S., Norman C., 2002, ARA&A, 40, 539

Savage R. S., Oliver S., 2007, ApJ, 661, 1339

Scargle J. D., 1998, ApJ, 504, 405

Sellke T., Bayarri M. J., Berger J. O., 2001, Am. Stat., 1, 62

Sivia D. S., 1996, Data Analysis: A Bayesian Tutorial. Clarendon Press, Oxford

Slezak E., Bijaoui A., Mars G., 1990, A&A, 227, 301

Starck J.-L., Murtagh F., 2006, Astronomical Image and Data Analysis. Springer-Verlag, Berlin

Starck J.-L., Pierre M., 1998, A&AS, 128, 397

Starck J.-L., Bijaoui A., Valtchanov I., Murtagh F., 2000, A&AS, 147, 139

Stewart I. M., 2006, A&A, 454, 997

Stewart I. M., 2009, A&A, 495, 989

Strong A. W., 2003, A&A, 411, L127

Szalay A. S., Connolly A. J., Szokoly G. P., 1999, AJ, 117, 68

Valtchanov I., Pierre M., Gastaud R., 2001, A&A, 370, 689

Vanden Berk D. E. et al., 2006, AJ, 131, 84

Vikhlinin A., Forman W., Jones C., Murray S., 1995, ApJ, 451, 542

Voges W. et al., 1999, A&A, 349, 389

Voges W. et al., 2000, Int. Astron. Union Circ., 7432, 1

von der Linden W., Dose V., Fischer R., 1997, in Sears M., Nedeljkovic V., Pendock N. E., Sibisi S., eds, Maximum Entropy and Bayesian Methods. NMB Printers, Port Elizabeth, p. 146

von der Linden W., Dose V., Padayachee J., Prozesky V., 1999, Phys. Rev. E, 59, 6527

von Toussaint U., Gori S., 2007, in Knuth K. H., Caticha A., Giffin A., Rodríguez C. C., eds, AIP Conf. Proc. Vol. 954, Bayesian Inference and Maximum Entropy Methods in Science and Engineering. Am. Inst. Phys., New York, p. 212

Wahba G., 2006, Spline Models for Observational Data. SIAM, Philadelphia

Watson M. G. et al., 2003, Astron. Nachr., 324, 89

White N. E., Giommi P., Angelini L., 1994, BAAS, 26, 1372

This paper has been typeset from a TEX/LATEX file prepared by the author.